Fresh Human Retinal scRNA-seq Atlas Reveals a Novel Cone Subtype and Cellular Diversity

Luning Yang[1], Yiwen Tao[1], Qi Pan[1], Tengda Cai[1], Yunyan Ye[2], Jianhui Liu[3], Yang Zhou[4], Yongqing Shao[5], Quanyong Yi[5], Zen Haut Lu[6], Lie Chen[6], Gareth McKay[7], Richard Rankin[8], Weihua Meng[1,9,10*]

1 Nottingham Ningbo China Beacons of Excellence Research and Innovation Institute, University of Nottingham Ningbo China, Ningbo, China, 315100

2 Department of Ophthalmology, Lihuili Hospital affiliated with Ningbo University, Ningbo, China, 315040

3 Department of Cardiology, Lihuili Hospital affiliated with Ningbo University, Ningbo, China, 315040

4 Ningbo Institute of Innovation for Combined Medicine and Engineering, The Affiliated Li Huili Hospital, Ningbo University, Ningbo, China, 315201

5 Department of Ophthalmology, The Affiliated Ningbo Eye Hospital of Wenzhou Medical University, Ningbo, China, 315040

6 PAPRSB Institute of Health Sciences, Universiti Brunei Darussalam, Bandar Seri, Begawan, Brunei Darussalam, BE1410

7 Centre for Public Health, Institute of Clinical Science, Queen's University Belfast, Block B, Royal Hospital, Grosvenor Road, Belfast, UK, BT12 6BA

8 School of Mathematical Sciences, University of Nottingham Ningbo China, Ningbo, China, 315100

9 Division of Population Health and Genomics, School of Medicine, University of Dundee, Dundee, UK, DD2 4BF

10 Center for Public Health, Faculty of Medicine, Health and Life Sciences, School of Medicine, Dentistry and Biomedical Sciences, Queen's University Belfast, Belfast, UK, BT12 6BA

Corresponding Author: Dr Weihua Meng

Address: Division of Population Health and Genomics, Ninewells Hospital and Medical School, University of Dundee, Dundee, UK, DD2 4BF; Nottingham Ningbo China Beacons of Excellence Research and Innovation Institute, University of Nottingham Ningbo China, Ningbo, China, 315100. Tel: +44 1382 383419; +86 574 88188632. Email: w.meng@dundee.ac.uk; weihua.meng@nottingham.edu.cn. ORCID: 0000-0001-5388-8494

ORCID codes

Luning Yang: 0000-0001-9056-5950

Yiwen Tao: 0009-0000-0102-4205

Qi Pan: 0000-0003-0135-9122

Tengda Cai: 0000-0003-1617-506X

Yunyan Ye: 0009-0005-2325-1405

Jianhui Liu: 009-0004-1341-0831

Yang Zhou: 0000-0001-9273-0489

Yongqing Shao: 0009-0006-1319-8521

Quanyong Yi: 0000-0002-9369-3998

Zen Haut Lu: 0000-0002-9408-0579

Lie Chen: 0000-0001-9764-4299

Gareth McKay: 0000-0001-8197-6280

Richard Rankin: 0000-0001-6445-2602

Weihua Meng: 0000-0001-5388-8494

Abstract

The human retina has a remarkable diversity of cell types, which is crucial for understanding the mechanisms underpinning visual development and function. While single-cell RNA sequencing (scRNA-seq) has advanced our understanding of retinal biology, most studies have relied on postmortem or frozen samples, potentially missing important transcriptional information. The aim of this study was to create the first comprehensive scRNA-seq atlas of fresh human retinal samples from living donors and recently deceased individuals using scRNA-seq technology. A total of 106,829 cells were analyzed, which were collected from nine retinal samples using standardized scRNA-seq workflow. Our findings identified several novel subtypes of known retinal cells, including new subgroups of cones and amacrine cells (ACs), each characterized by distinct gene expression profiles. Notably, we discovered a novel cone subtype, the ELF1-Cone, which shows a clear developmental trajectory from mlCone precursors. This subtype exhibits unique functional properties and metabolic profiles, regulated by key transcription factors ELF1 and PRKAA1. We also identified five distinct AC subtypes, including three GABAergic ACs, each with unique gene expression profiles and functional characteristics. Our study highlights the critical importance of using fresh human retinal tissue for accurate cellular mapping and trajectory inference. Significant differences were observed between fresh and postmortem retinal samples in terms of pseudo time analysis such as RNA velocity. We also performed a comparative analysis of diabetic without retinopathy, diabetic retinopathy, and non-diabetic samples, suggesting diabetes-related transcriptional variation. In conclusion, we present a comprehensive human retina atlas using fresh samples that contribute to existing knowledge of retinal cell diversity, function, and transcriptional profiles. Our study is a milestone for future studies that will improve understanding of retinal biology and disease mechanisms.

Keywords: Single-cell RNA sequencing; Human retina; Transcriptomic atlas; Fresh tissue analysis; Retinal cell types

Introduction

The human retina is a complex and vital component of the eye that plays a crucial role in light capture and the initiation of the vision process [1]. As a highly specialized neural tissue lining the back of the eye, the human retina detects and converts incoming light into electrical signals, forming the foundation of visual perception and interpretation of our surroundings [2]. In general, the retina consists of photoreceptors (rod and cone), signaling neurons (bipolar, horizontal, amacrine, and retinal ganglion cells), and supporting cells (müller glial cell, microglia, astrocyte) [3]. Each cell type differs in its morphology, functionality, and subtype composition [4]. The retina's complex structure and function enable humans to process visual information from our environment [5]. However, many questions remain of the structure and function of the human retina [3]. The complex composition of the human retina also makes it vulnerable to various diseases that can significantly impact vision and quality of life, highlighting the importance for improved understanding of the retinal structure and function for the development of effective treatments and preventive measures [6].

Researchers have adopted advanced sequencing technologies to overcome these challenges and gain deeper insights into retinal biology and disease pathology. Single-cell RNA sequencing (scRNA-seq) provides in-depth analysis at the single cell level and is particularly valuable for studying retinal diseases like age-related macular degeneration and diabetic retinopathy that progress in a heterogenous manner [7, 8]. scRNA-seq enables efficient identification of cell type-specific expression patterns, analysis of disease progression stages within the same sample, and exploration of cellular heterogeneity in both physiological and pathological states. In 2019, Lukowski et al. revealed 18 distinct clusters of retinal cells using scRNA-seq, significantly contributing to our understanding of retinal cell diversity [9]. In 2020, Farjood et al. identified subpopulations within retinal pigment epithelium cells, including

a group with stem cell-like properties, highlighting their heterogeneity through scRNA-seq [10]. Voigt et al. utilized scRNA-seq to find distinct glial populations in degenerating retinas, emphasizing transcriptomic changes in retinal diseases [11]. Collectively, these studies underscore the utility of scRNA-seq in unraveling the cellular and molecular landscapes of the human retina. In addition, single-nucleus RNA sequencing (snRNA-seq) has gained traction in human retinal studies. By 2023, Wang et al. used snRNA-seq to demonstrate the intricate regulatory mechanisms in retinal cells, particularly transcription factor collaborations affecting gene regulation [12]. Most recently, Liang et al. combined single-cell RNA and assays for transposase-accessible chromatin using sequencing to create a comprehensive reference atlas from 2.4 million cells, integrating transcriptome and chromatin accessibility data to unveil over 110 cell types and their regulatory networks using snRNA-seq [13].

Unlike scRNA-seq, snRNA-seq can be performed on frozen or archived retinal tissues, which is particularly valuable where the availability of fresh human retinal tissue is limited [14]. The reliance on frozen samples is largely due to the challenges associated with acquiring, preprocessing, and storing human retinal tissue [12]. These challenges encompass not only technical issues but also ethical considerations, such as the difficulty of obtaining fresh samples from living donors [15, 16]. Importantly, snRNA-seq fails to sufficiently capture RNAs localized in the cytoplasm, which are important for understanding post-transcriptional regulation and cellular processes in the retina [17]. A 2009 study by Botling et al. examined the impact of thawing on RNA integrity and gene expression analysis in fresh frozen tissue [18]. They found that the kinetics of RNA degradation after thawing are likely to be tissue specific. This finding is supported by more recent research, including a 2023 review by Thakral et al., which noted that early postmortem interval (PMI) studies on eye tissue found that the type of tissue samples used for early and late PMI had an impact on the stability of RNA post-mortem

[19]. This leaves a gap in the field of human retinal research: the lack of atlases for comprehensive scRNA-seq analysis of fresh human retinal samples from living donors, particularly given the fact that fresh tissue better reflects the *in vivo* cellular transcriptional status more accurately than postmortem or cultured samples [20].

scRNA-seq offers unique advantages for retinal studies, capturing both nuclear and cytoplasmic RNAs and enabling the exploration of functional responses in live cells. This technique allows for the analysis of freshly isolated cells while maintaining their viability and function, providing crucial insights into the dynamics of cellular processes such as metabolic activity and stress responses [21]. Moreover, scRNA-seq can track changes in cell states over time, which is essential for understanding the progression of conditions like diabetic retinopathy [22, 23].

It is worth noting that while previous studies have created retinal atlases and some have used unfrozen postmortem tissue samples, our study is among the first to explicitly focus on and demonstrate the critical importance of using fresh, living human retinal tissue for creating a comprehensive atlas. By directly comparing fresh and postmortem samples, we provide unique insights into the advantages of using living tissue in retinal research, building upon and extending previous work in this field. We have integrated scRNA-seq data from nine samples, encompassing samples from both living donors and recently deceased individuals (retina were collected within several hours of death). This approach enables a high-quality and comprehensive representation of retinal cell types and states, building upon and extending previous eye atlases that have focused on specific ocular cell types and those derived from frozen necropsy sources. Our atlas aims to provide a deeper understanding of retinal biology and disease mechanisms, with potential applications in developing targeted therapies for various retinal disorders. As some of the samples included are from donors with diabetes, we have also included a

comparative analysis between non-diabetic, diabetic without retinopathy, and diabetic retinopathy samples to differentiate the characteristic patterns and cell type distributions.

Materials and Methods

Retinal tissues from fresh human donor eyes and cadaveric donor eyes

Human retinal tissues were collected from the Lihuili Hospital (affiliated with Ningbo University) and the Ningbo Eye Hospital (affiliated with Wenzhou Medical University) from June 1, 2023, to May 31, 2024. Study ethics was approved separately by the ethics committees for Lihuili Hospital, the Ningbo Eye Hospital, and the University of Nottingham, Ningbo, China. Retinal samples were collected following written informed consent from two patients attending the Lihuili Hospital following enucleation due to medical conditions, and seven samples were collected from the Ningbo Eye Hospital. Of the seven samples collected from the Ningbo Eye Hospital, two pairs of eyes were collected from recently deceased cadavers, and three from patients following enucleation for medical reasons. Detailed information of the nine samples is shown in Table 1.

Single-cell RNA sequencing (lab preparation)

Retinal tissue was prepared for scRNA-seq using the Dissociation Kit (LK003150-1bx manufactured by Worthington Biochemical Corporation). Tissue was dissociated, filtered, and treated with red blood cell lysis solution (130-094-183, Miltenyi Biotec). Cell viability was assessed using CountStar, and viable cells were enriched using the Dead Cell Removal Kit (130-090-101, Miltenyi Biotec).

The scRNA-seq libraries were prepared using a total of 10,000 cells per sample. The Chromium Single Cell 3' Library and Gel Bead Kit V3.1 (10X Genomics, PN1000268) was used to create emulsified

single-cell gel beads. Following cell lysis, primers comprising poly-T, barcodes, unique molecular identifiers (UMIs), and a 'read 1 primer sequence' in gel bead-in-emulsion (GEM) were used to reverse-transcribe RNA. The addition of sample index and 'read 2 primer sequence' was performed through adapter ligation. Following quality control, libraries were 150 bp paired-end nucleotide sequenced using the Illumina NovaSeq platform. Reads were constructed from raw BCL files using Illumina's bcl2 FASTQ converter. Quality control parameters included: had >3 read sequences; > 20% of bases had a quality rating of < 5; and adapter sequence detected.

Generation of single cell data

The 10X Genomics Cell Ranger V8.0.1 pipeline (https://support.10xgenomics.com/single-cell-gene-expression/software/pipelines/latest/what-is-cell-ranger) was used with default parameters to demultiplex and map raw data to the reference genome (GRCh38-2024-A). Alignment, filtering, barcode counting, and UMI (unique molecular identifier) counting were all done by Cell Ranger count on FASTQ files which generates feature barcode matrices using the chromium cellular barcodes, Cell Ranger count, and gene expression algorithms.

Quality control and doublets removal

For each sample, 10X Genomics Cell Ranger created raw and filtered feature-barcode matrices. Quality control and doublet removal were conducted separately for each dataset to remove and enrich low-quality and enrich high-quality cells, respectively. DoubletFinder (https://github.com/chris-mcginnis-ucsf/DoubletFinder) was used to eliminate doublets. Subsequently, cells of high quality were selected using the Seurat R package (v5.1.0) [24], according to the following

quality control criteria: cells with a gene count > 200, UMI count > 400, and a mitochondrial read count proportion < 20% were retained.

Cell clustering and dimensionality reduction

Scanpy (v1.10.2) [25] was used to analyze the scRNA-seq data. Raw counts were log-normalized, and 5,000 highly variable genes were selected. The scVI model from the scvi-tools package (v0.17.1) [26] was trained using the raw counts of these highly variable genes for dimension reduction and batch correction. Using the 20 resultant latent dimensions, a *k*-nearest neighbors (KNN) graph was created for Leiden clustering and uniform manifold approximation and projection (UMAP) visualization.

Iterative Leiden clustering with parameters of 0.05 to 1.0 was employed to identify cellular partitions within the dataset. In each iteration, a new KNN graph was generated, and Leiden clustering was applied to the scVI batch-corrected latent representation. The calculation of silhouette scores for Leiden clustering at increasing resolutions of 0.1 provided optimal clustering resolution for the scRNA-seq data. The clustering quality for each resolution was assessed using scikit-learn, and the resolution with the highest silhouette score was chosen to identify the most distinct and significant clusters. This was further verified by UMAP plots and cell type specific marker gene expression to ensure the resolution chosen provided the most well-defined and meaningful clusters, enabling the assignment of the first-level annotation of major cell classes. Cells were then divided into smaller groups, and the steps were repeated to finalize subcluster cell type annotations. Subclusters were identified and labeled using known marker genes, differential expression (DE) analysis, and comprehensive enrichment analysis. The optimal cluster resolution for each group was determined by these results and the corresponding silhouette score.

Differential expression (DE) analysis

The $FindMarkers$ function in Seurat was utilized to identify differentially expressed genes (DEGs) across each retinal cell class. The Wilcoxon rank-sum test was applied, considering only genes detected in at least 25% of cells in either population, and statistical significance was determined by calculating unadjusted and adjusted p values.

DEGs were categorized as upregulated or downregulated based on whether their average log2 fold change (avg_log2FC) was positive or negative, respectively. Further classification was performed based on the magnitude of the log2 fold change, with those having $|avg_log2FC| > 1$ labeled as 'Highly' and those with $|avg_log2FC| \leq 1$ labeled as 'Lowly'. A composite label was generated by combining the up/down status with the high/low classification.

Similar DEG analysis was conducted for subclusters of amacrine cells (ACs), bipolar cells (BCs), and cones, using the same parameters and methodologies. Top DEGs were selected for display by identifying the top five upregulated and the top five downregulated genes for each cell type. This approach ensured a robust identification and categorization of DEGs across different cell classes and subpopulations.

Pathway enrichment analysis

Pathway enrichment analysis was conducted using multiple approaches to comprehensively assess biological processes across different cell types and conditions. Gene Set Variation Analysis (GSVA) was performed using the GSVA R package [27] to evaluate pathway activity, utilizing hallmark gene sets from the molecular signatures database (MSigDB) of homo sapiens. Gene Ontology (GO)

enrichment was conducted using ClusterProfiler (https://github.com/YuLab-SMU/clusterProfiler) to identify significantly enriched pathways for DEGs in each cluster. The "clusterProfiler" R package was utilized to perform these analyses and visualize the results, considering p values below 0.05 as indicative of significant pathway enrichment.

Additionally, the "irGSEA" R package (https://github.com/chuiqin/irGSEA/) was used to score individual cells through a multi-genomic enrichment approach, generating a comprehensive multi-genomic enrichment scoring matrix. DE analysis within this matrix was then conducted for each cell class and cell type using the Wilcoxon test, providing a detailed evaluation of gene expression variations.

SCENIC and cell-type specificity index analysis

The SCENIC R package was used to identify transcription factor (TF) regulons specific for each cell type using human retinal cones. The raw count gene expression matrix of cones processed with previous quality control steps was used as the input data. After retaining genes with at least three counts and expressed in over one percent of total cells, we used GENIE3 to perform correlation analysis and TF-target correlation assessment. Co-expression modules were identified and refined into regulons based on DNA-motif analysis. Two complementary regulatory region databases were utilized: one encompassing region 10 kb upstream and downstream of transcription start sites, and another focusing on 500 bp upstream and 100 bp downstream, both from the hg38-RefSeq-r80 genome annotation. Regulon activity scores were later calculated using AUCell, followed by binarization to determine the activity state of each regulon in individual cells.

Following the SCENIC analysis, the cell-type specificity index (CSI) analysis was applied to identify

and characterize transcriptional regulatory modules. It was based on regulon activity scores derived from the SCENIC output. CSI quantifies the similarity of regulon activity patterns across cells, enabling the identification of co-regulated gene sets with values ranging from 0 to 1. Higher CSI values indicate greater specificity in co-regulation. We applied a CSI threshold of 0.5 to focus on strongly co-regulated regulons. The resulting CSI matrix was hierarchically clustered using Ward's method to identify modules of co-regulated genes.

Dynamo analysis

We used Velocyto [28] to generate spliced and unspliced expression matrices from Cell Ranger output files. These two matrices, along with the raw expression matrix, were imported into Dynamo [29], a python package for RNA velocity analysis. Data preprocessing included normalization and dimension reduction. Gene-specific velocity dynamics were calculated, and RNA velocity-derived metrics were generated, including speed, acceleration, divergence, and ddhodge potential.

CellOracle simulation analysis

We use CellOracle [30] to perform silico pertubation analysis to simulate gene knockout of ELF1 and PRKAA1 and corresponding effects on cell steate transitions, which are key TFs selected from gene regulatory network analysis. Additionally, pseudotime analysis is performed to infer developmental trajectories after the knockout. All the simulation and calculation were built based on the TF regulatory network generated from the SCENIC output of the human retinal cone dataset.

Cell communication analysis

Cell-cell communication analysis was performed using the CellChat [31] package in R, focusing on "Secreted Signaling" and "Cell-Cell Contact" interactions. Data preprocessing steps involved subsetting to signaling genes, identifying overexpressed genes and interactions, and projecting data onto a protein-protein interaction network. Communication probabilities were computed, filtered, and aggregated into a network. We focus on the interaction activities between cone cell types: ELF1-Cone, mlCone, and sCone.

Differential expression analysis by cell class in diabetes

EdgeR [32] was used to detect DE analysis of diabetes comparisons. Based on their diabetic conditions, the nine retain samples were divided into three states: donors without diabetes, donors with diabetes with no diabetic retinopathy, and donors with both diabetes and diabetic retinopathy as shown in Table 1. When performing DE analyses, individual cells were categorized into two groups. The control group was composed of non-diabetic datasets, and the test group was composed of diabetic datasets and diabetic retinopathy datasets. A negative binomial generalized log-linear model was used to analyze the gene counts, taking the covariates of major cell class and diabetic status. The model was fitted using the glmQLFit function.

Odds ratio (OR) analysis of cell type distribution in diabetic vs. non-diabetic samples

Odds ratios (OR) were computed using the methodology described in Zheng et al. [33] in order to characterize the cell type and subtype preference distribution between the diabetic without retinopathy group (DM), the non-diabetic group (nonDM), and the diabetic retinopathy group (DR). Using the Benjamini-Hochberg (BH) approach, p values were modified after being determined using Fisher's

exact test. An OR > 1.5 and adjusted p value < 0.05 indicates a cell type/subtype is more likely to be dispersed in this group, while an OR < 0.5 and adjusted p value < 0.05 indicates a less likely distribution.

Results

Single-cell transcriptomic atlas of fresh human retina from living and cadaveric donors

We aimed to develop a comprehensive human retinal single-cell transcriptomic atlas, particularly focusing on fresh samples of the human retina. Five samples from living individuals and two paired samples from recently deceased individuals were collected. These samples were further categorized based on their diabetic status into three groups: nonDM (size = 4), DM (size = 3) and DR (size = 2). After quality control using Seruat package, a total of 106,829 cells were obtained for further analysis. The clustering results of the nine samples with different resolution levels are shown in Figure 1, and the resolution of 0.3 was chosen as the best value.

Based on the cell ontology, the annotation levels were split into two levels. The first level is the cell classes, they were first annotated based on the known markers of retinal cell types reported previously [34]. The corresponding cell clusters were assigned the identities (Figure 2A), including AC (TFAP2B/SLC32A1), astrocyte (GFAP), cone (ARR3/GNAT2/GNGT2), rod (RHO/PDE6G/GNGT1), müller glia cell (RLBP1), horizontal cells (LHX1/TNR), BC (NETO1), retinal ganglion cells (SLC17A6/RBPMS), microglia (CD74/TYROBP/C1QA), and T cells (CD69/CD52/CD3D) (Figure 2B).

Most of the major cell types exhibited well-isolated, tight clusters (Figure 3A). In addition, cluster heterogeneity is visible for some cell classes with multiple types, such as BCs. The ACs, astrocytes,

BCs, cones, horizontal cells, T cells, microglia cells, müller glia cells (MGCs), and rods were detected in all the analyzed datasets, and retinal ganglion cells (RGCs) were detected in four donors (3, 4, 6 and 7). For all the datasets, rod photoreceptor cells were the most abundant major type, followed by MGCs and BCs (Figure 3B and Table 2). Gene set variation analysis (GSVA) plots are used to show the terms of the hallmark gene set enrichment pathway for each identified cell population, using the upregulated and downregulated gene sets shown in Figure 2C. The enrichment pathways align with known biological functions, further supporting the annotation of major retinal cell types (Figure 4). For example, microglia show significant enrichment in inflammatory and immune-related pathways, consistent with their role as the primary immune cells in the retina. MGC show enrichment in glycolysis, supporting their known role in metabolic support of neurons.

In all datasets, all the markers showed quite distinct and expected distribution among the cell types. To further accurately annotate the cell types, we performed a second round of annotation specifically for the clusters that contained ACs, horizontal cells, RGCs and also for the clusters that contained astrocytes and MGCs, respectively.

There were challenges in differentiating between ACs, horizontal cells, and RGCs from the scRNA-seq retinal samples given their shared developmental trajectory and similar transcriptional profiles. These three cell types are all derived from a common pool of retinal progenitor cells (RPCs), and data generated from murine Atoh7-null retinas indicated genes associated with RGCs, ACs, and horizontal cells were expressed in a highly overlapping fashion making it challenging to separate these cell types into distinct clusters following scRNA-seq analyses [35]. Furthermore, the genesis of ACs and horizontal cells is also controlled by Foxn4 by regulation of the expression of retinogenic factors that are involved in their fate commitment [36]. As such, the clusters composed of ACs, horizontal cells,

and RGCs were further trained by the scVI model and Leiden clustered, which assigned their identities based on specific markers as shown in Figure 5A-C, with corresponding dot plots and dendrogram heatmaps (Figure 5D, E), and the final annotation results are shown in the UMAP plot (Figure 5F).

The macroglia cluster was composed of astrocytes and MGCs which provide essential support functions in the retina and share similar transcriptional profiles [37]. Both cell types are also reactive in response to retinal injury [38, 39]. MGCs represent the predominant glial cells in the retina and are present in large numbers throughout the retinal layers [38], with the relative high abundance making it harder to capture the astrocytes. In this situation, the clusters composed of astrocytes and MGCs were further trained by the scVI model and Leiden clustered, and assigned their identities based on specific markers with corresponding dot plots and dendrogram heatmaps (Figure 6B), and the final annotation results are shown in the UMAP plot (Figure 6A). Our approach was able to successfully differentiate the distinct transcriptional profiles for the various retinal cell types highlighting the intricate cellular diversity within the human retina.

Bipolar cells

Retinal bipolar cells receive synaptic input from photoreceptors and process it in diverse ways before transmitting an input to RGCs. They are essential components of the human retinal circuitry, serving as intermediaries between photoreceptors and RGCs. Their diverse subtypes and molecular characteristics allow for complex processing of visual information, including light adaptation, temporal frequency processing, and contrast detection. Understanding bipolar cell function is crucial for comprehending retinal development, visual processing, and the pathogenesis of certain retinal diseases.

BCs can be subdivided on the basis of two main distinctions: rod versus cone BCs and ON versus OFF BCs, as shown in Figure 7A. The former is associated with synaptic input, while the latter distinguishes the signaling mechanism in dendrites and the level of axonal stratification [40].

The ON BC subtypes, such as DB5, DB6, BB+GB, and IMB, respond to light onset and transmit signals via mGluR6 receptors [41]. OFF BC subtypes, including DB1, DB2, DB3a, DB3b, FMC, and OFFx, hyperpolarize in response to light offset, utilizing ionotropic glutamate receptors (AMPA and Kainate) [42]. RBCs are crucial for scotopic (low-light) vision, transmitting signals from rod photoreceptors primarily to AII ACs, which then relay the information to cone BC cells and ultimately to RGCs [43]. This classification highlights the diverse roles and pathways of BCs in visual processing.

DB4 cells are mostly classified as ON BC in the retina, however, some studies have ambiguously categorized DB4 as OFF BC [44]. To further characterize this group, we identified a high-level expression of GRM6 in DB4 clusters in our study, a key component of the ON BC signaling pathway. mGluR6 detects a decrease in glutamate, which then initiates a signaling cascade that depolarizes ON BCs. On that basis, we confirmed the attribution of this DB4 cluster to ON BCs.

To delineate the landscape of BCs, we isolated BCs and performed scVI model training and Leiden clustering based on suitable resolution levels. BCs were divided into subtypes previously characterized by common marker genes for each BC subpopulation across all the datasets (Figure 7B, C). A total of 6 ON BC and 5 OFF BC subclusters were identified in the human datasets (Figure 7D).

Amacrine cells

Retinal amacrine cells play a complex role in visual signal processing, forming synapses with multiple cell types, including BCs, RGCs, and other ACs, providing both feedback inhibition to BCs and feedforward inhibition to RGCs, shaping the visual signal [45, 46]. There are numerous types of ACs, each with potentially different patterns of connectivity and roles in signal processing, that use various neurotransmitters, including GABA.

Most ACs are inhibitory neurons utilizing GABA or glycine as neurotransmitters [34]. After retraining the clustering model by assessing the expression of marker genes for GABAergic (GAD1 and GAD2) and glycinergic (SLC6A9) ACs, we identified three clusters with high GABA marker expression, with high DEGs MEIS2/BASP1, SOX5/PCP4, and CCDC39/RBFOX1 (Figure 8A-B). We inferred they are GABA ACs with distinct characteristics and functions. One cluster was represented by high SLC6A9 expression, annotated as Glycinergic ACs (GlyACs). Another cluster was represented by mid-levels of expression for all the three genes, which may correspond to a mixture of both GABA and glycine AC types with a role as intermediate ACs.

To further verify the function of the three different GABAergic ACs, we employed integrative irGSEA to score each cluster using a multi-genomic enrichment approach. We performed GO enrichment analyses for each cluster (Figure 8C-D). Except the GlyACs and intermediate ACs, the results of pathway analysis of these three different GABAergic ACs demonstrate that they have distinctly different functions. GABA-AC1 displays a unique focus on postsynaptic specialization and photoreceptor interaction. As indicated by the pathways “glutamatergic synapses” and “synaptic membranes”, these cells are enriched in pathways indicative of complex and diverse synaptic connections, including inhibitory (GABAergic) and potentially excitatory (glutamatergic) synapses. They play a crucial role in fine-tuning synaptic signaling and neurotransmitter release, as highlighted

by the pathways "regulation of trans-synaptic signaling" and "modulation of chemical synaptic transmission". Structurally, they are characterized by "distal axons" and "growth cones", suggesting that they are specifically adapted to synaptic interactions. GABA-AC1 are the highest involvement in developmental processes in GABA-ACs. GABA-AC2 enrichment pathways show focus on postsynaptic specialization and photoreceptor interaction. Pathways include postsynaptic density and postsynaptic specialization, suggesting a role in fine-tuning synaptic inputs. The cluster is also closely associated with photoreceptor outer segments and various types of cilia and is involved in eye development and visual system development. GABA-AC3 demonstrate a pronounced specialization in ion channel activities and calcium signaling. They are enriched in various ion channel activities, particularly voltage-gated and monoatomic ion channels. The strong emphasis on calcium ion transport and regulation of membrane potential suggesting a key role in rapid signal modulation. This subtype also shows significant involvement in synapse organization and regulation of trans-synaptic signaling, indicating a role in shaping synaptic communication. In summary, the novel GABA AC subpopulations identified in this study may represent specific modulators characterized by specialized roles in retinal function.

Cone photoreceptor cells

We identified four clusters of cones that correspond to distinct cell states, referred to as mlCone, sCone, ELF1-Cone and a cluster associated with corneal repair. Cones are classified based on their sensitivity to different wavelengths of light, which enables color perception. The three types of cones are sCones, which are sensitive to short wavelengths corresponding to blue light; mCones, which respond to

medium wavelengths corresponding to green light; and lCones, which are sensitive to long wavelengths corresponding to red light. [47].

Traditionally, cone cells have been classified as mlCones (medium/long-wavelength) and sCones (short-wavelength) due to the difficulty in distinguishing mCone and lCone[34]. We retrained the clustering model with annotation based on the expression patterns of key markers (Figure 9A). The mlCones and sCones were comprehensively identified based on high expression levels of OPN1LW, OPN1MW, and OPN1SW (Figure 9B). mlCones exhibit lower ARR3 expression compared to sCone. Additionally, mlCones were found to consist of two distinct clusters, differentiated by the expression of MGST3/GNB3 and KCNIP4/CNGA1.

We also identified a distinct cell cluster characterized by low ARR3 expression and high levels of KCNB2, and EYS (Figure 9C). We named this cluster ELF1-Cone. To determine the identity and function of ELF1-Cone, we performed pseudo-bulk differential expression analysis for each cluster including mlCone, sCone, ELF1-Cone and the corneal repair cluster.

Corneal repair cluster in cone photoreceptor

The corneal repair cluster was predominantly present in corneal ulcer sample (80.74%), exhibiting upregulation of genes critical for protein synthesis and cellular stress response. The top ten DEGs in the cluster including RPLP0, RPL13A, RPL6, and EEF1G (Figure 10A). RPLP0 is an important component of the ribosomal stalk, its high expression suggests an increased capacity for protein synthesis required for cellular repairments. This upregulation may indicate that cells in this cluster actively respond to injury by producing proteins necessary for corneal repair and regeneration.

RPL13A functions not only as a ribosomal protein but also in the interferon-γ-activated inhibitor of translation (GAIT) complex, which regulates the selective translation of certain mRNAs during inflammation. Up-regulation of RPL13A may reflect a dual role in both general protein synthesis supporting the repair process in this cluster and regulating specific inflammatory responses in corneal cells. Upregulation of EEF1G, part of the elongation factor-1 complex involved in the transport of aminoacyl tRNAs to ribose, suggests enhanced protein synthesis under stress conditions and activation of cell survival pathways in response to corneal injury. Increased expression of RPL4 and RPL6, important components of the 60S ribosomal subunit, further supports the hypothesis that these cells have an increased capacity for ribosome biogenesis and protein synthesis. Notably, this cluster may also have been affected by contamination of corneal ulcer from donor 5, reflect the introduction of non-retinal cells from damaged corneal tissue.

ELF1-Cone is discovered as a new subtype of cone photoreceptor

The top ten up-regulatory DEGs of ELF1-Cone including ASIC2, MSR1, and FRMD4A (Figure 10A). ASIC2 is an ion channel activated by extracellular acidification that may contribute to neuroprotective mechanisms and pH sensing in the retinal microenvironment. MSR1 is commonly associated with immune function and is capable to clear cellular debris. It plays a role in the removal of oxidized lipids and cellular debris, contributing to tissue homeostasis. FRMD4A is involved in cytoskeletal organization and cellular polarity and may potentially contribute to efficient signaling of this cluster. We propose a functional hypothesis for this unknown cone cluster, where cone cells have a unique adaptive capacity to sense and respond to changes in the retinal microenvironment, maintain

specialized cellular structures critical to their function, and provide neuroprotection against oxidative stress and other cellular threats.

To further validate the functions of the ELF1-Cone cluster, we performed GSVA and GO analyses as shown in Figure 10B-C. There were significant enrichments of energy metabolic processes, including oxidative phosphorylation, aerobic respiration and cellular respiration. It was also supported by the enrichment terms of mitochondrial components and energy-related processes. The enrichment results supported that ELF1-Cone cells have a high capacity for energy production, which is also essential for maintaining their specialized function in the retina. The enrichment of cytoplasmic translational and ribosomal components protein synthesis pathways suggesting an active protein production machinery. This allows ELF1-Cone cells to respond rapidly to changing conditions or stressors in the retinal microenvironment. GSVA heatmaps show high activation of the *hallmark_apical_surface* and *hallmark_apical_junction* pathways in ELF1-Cone cells, suggesting a specific role in cell-to-cell interactions and maintenance of retinal retina, indicating a specific role in intercellular interactions and maintenance of retinal organization. Activation of *hallmark_hedgehog_signaling* further implies involvement in cell differentiation and organization patterns. GO analysis also revealed an enrichment of transmembrane transporter protein activity and various binding processes, suggesting enhanced cell signaling and metabolite exchange. The presence of adhesion spots and cell-matrix junction terms is consistent with GSVA results, emphasizing the importance of cell-matrix interactions in ELF1-Cone function.

ELF1 and PRKAA1 are key TFs in ELF1-Cone

On this basis, for further experimentation and validation, we performed SCENIC analysis to profile cell

state specificity and TF activity (Figure 10F). The top 40 regulons are listed in supplementary Table S1. ELF1 is a transcription factor involved in the regulation of T-cell specific genes. SETDB1 is a histone methyltransferase that specifically trimethylates lysine 9 of histone H3 and is also associated with retinal development and photoreceptor maintenance. RCOR1 is a transcriptional co-repressor involved in neuronal gene silencing and plays a role in retinal progenitor cell differentiation. SREBF1 is a TF that regulates genes involved in lipid metabolism. The presence of genes such as RCOR1, SETDB1, and SREBF1 in the ELF1-Cone cluster suggests unique metabolic and developmental features and gene regulatory networks compared to other optic cone cell types. Based on the list of genes, we could infer the TFs involved in the following processes: transcriptional regulation (ELF1, ETV3, STAT5B, TBP) chromatin modification (SETDB1, PHF8, RBBP5) metabolic processes (SREBF1, PRKAA1) DNA repair (XRCC4). These findings are consistent with GO analysis, particularly highlighting the enrichment of pathways regulated by TFs and those involved in metabolic processes.

At the same time, we use the connection specificity index (CSI) to perform regulon module analysis. The results identify four distinct groups of regulons in cones, ordered from module one to module four. Key TFs of ELF1-Cone were labeled and observed to aggregated in module two and module four, corresponding to two different characteristic regulon groups (Figure 10D-E). Module two was enriched with TFs involved in chromatin modification (SETDB1, PHF8, RBBP5), transcriptional regulation (ELF1, ETV3, STAT5B), and cell cycle control (E2F6). Module four was associated with metabolic regulation (SREBF1, PRKAA1), DNA repair (XRCC4), and general TFs (TBP, TAF1). This indicates the function of ELF1-Cone mainly including two aspects. The ELF1-Cone key TFs in module two supported its role in epigenetic regulation and cell fate determination, which could be crucial for maintaining self-identity. The ELF1-Cone key TFs in module four supported its involvement in

metabolic processes and cellular stress response, potentially reflecting the high energy demands and light-induced stress in cone cells. While further experimental validation is needed, this transcriptional profile indicates that ELF1-Cone cells could play specialized roles in retinal function, potentially including rapid cellular adaptation to changing light conditions and enhanced neuroprotective capabilities.

Cell Trajectory inference of ELF1-Cone

Dynamo is applied to study cellular dynamics, gene regulatory networks of ELF1-Cones, and revealed a potential developmental trajectory from mlCone to ELF1-Cone. This method builds on and extends the concept of RNA velocity, utilizing the ratio of unspliced to spliced mRNAs to predict the future state of individual cells. We divided our nine datasets into three groups to perform Dynamo analysis: all samples combined (including both fresh and cadaveric), fresh samples from living donors only, and cadaveric samples without freezing. The analysis was visualized using consistent UMAP reduction to reveal distinct cellular dynamics across conditions. As shown in Figure 11A, the all sample shows distinct clusters for CR, mlCone, ELF1-Cone, and sCone, with clear transitions between them, particularly from mlCone to ELF1-Cone. In the fresh living sample condition, we observe a more pronounced and directional flow from mlCone to ELF1-Cone. The transitions appear clearer and more defined, suggesting that in fresh samples, the differentiation pathway from mlCone to ELF1-Cone is more evident and potentially more active. The velocity flow is particularly evident at the boundary junction, highlighting that this differentiation pathway is strong and direct in the fresh sample. However, in the condition of cadaveric samples, the flow patterns become more chaotic and less directional. The transition from mlCone to ELF1-Cone is less clear, and the overall organization of the

clusters appears more diffuse. This suggests that post-mortem changes may disrupt the normal differentiation processes and cellular state.

The cellular dynamics analysis in Figure 11B provides further insights into the state of ELF1-Cone in fresh living datasets. The ELF1-Cone region is of moderate to high-speed indicating active transitions. The low divergence also suggesting that cells are converging to a specific state rather than branching into different fates. The low to moderate acceleration and curvature in the ELF1-Cone region suggest ongoing changes in cell state, but with relatively simple developmental trajectories.

To further verify the function of ELF1-Cones, we performed CellOracle to simulate the effects of knocking out specific TFs on the developmental trajectories of cones. ELF1 is the key TF for ELF1-Cone with the highest residual sum of squares (RSS) rank in regulon list, plays a significant role in the transcriptional program. PRKAA1, while lower in the rankings, could be crucial for regulating the distinct metabolic profile observed in ELF1-Cones, given its known role in energy homeostasis and the enrichment of metabolic processes in these cells. We used CellOracle to elucidate the exact functions of these factors in ELF1-Cone cells and their potential contributions to the unique characteristics of this cell type.

As shown in Figure 11C, there were significant changes in the flow patterns: the original cones from the living fresh samples showed clear directional flows, particularly from the mlCone towards the ELF1-Cone. The flows were well-organized and consistent, indicating a stable developmental trajectory. After knocking out of ELF1, the directional flow from mlCone to ELF1-Cone was disrupted and there was an increase in turbulent flows, particularly in the central regions. Some areas showed reversed flows compared to the original dataset. It indicates that ELF1 plays a crucial role in maintaining the normal differentiation pathway from mlCone to ELF1-Cone. Its absence leads to a loss of directional

development and potentially affects cell fate decisions. The perturbation simulations of PRKAA1 knockdown showed even more dramatic changes. There's a significant increase in the magnitude of flows across the entire plot. The flow patterns become highly chaotic, with many conflicting directions. The organized structure seen in the fresh datasets is almost completely lost. This implies that PRKAA1 has a broader influence on cellular dynamics, possibly affecting multiple aspects of cell metabolism and signaling. Its knockout appears to destabilize the entire system, leading to unpredictable cellular behaviors. ELF1 knockout primarily affects the mlCone to ELF1-Cone transition, while PRKAA1 knockout has a more global effect on cellular dynamics.

Cell to cell interaction inside cones

CellChat analysis revealed complex interactions between ELF1-Cones, mlCones and sCones as shown in Figure 12. Key interactions include NEGR1, CADM1 and CDH2. NEGR1 is known to be involved in cell adhesion and neurite outgrowth. CADM1 and CDH 2 are important for synaptic organization and intercellular adhesion, and is often involved in neural organization. It indicates a critical role in maintaining the physical organization between ELF-Cones and mlCones, and in maintaining specific synaptic connections between these subtypes. Suggesting ELF1-Cones are in a state of active communication while maintaining a relatively stable identity.

Horizontal cells

The human retina predominantly contains two horizontal cell subtypes, H1 and H2 [48]. In our study, we identified both horizontal cell types based on the high expression levels of LHX1 and ISL1, respectively (Figure 13).

Diabetic and non-diabetic comparative analysis

The annotated cell type proportions for each sample are presented in Table 2. Significant variability was observed across samples, with donors 01, 06, and 07 showing notably atypical cellular compositions. Donor 01 (76-year-old diabetic male, corneal staphyloma) was characterized with high levels of microglia (22.55%) and low rods (42.76%), suggesting diabetes-related inflammation. Donor 06 (50-year-old non-diabetic female, eyeball atrophy) showed elevated BCs (23.24%) and microglia (13.98%), indicating possible selective cell survival. Donor 07 (68-year-old non-diabetic female, corneal perforation) had the highest MGCs (26.21%) and lowest rods (40.15%), suggesting reactive gliosis. These three samples were excluded from subsequent comparative analyses between diabetic retinopathy (DR), diabetes mellitus (DM), and non-diabetic (nonDM) groups to investigate disease-specific retinal cell population variation. Figure 14A illustrates the cell proportion distributions for the three groups using boxplots.

To explore the differences in single-cell RNA profile patterns of major cell types and subtypes in those with diabetes and diabetic retinopathy, we applied a comprehensive compositional analysis. This included DE analysis using a negative binomial generalized log-linear model, odds ratio (OR) analysis to identify cell types or subtypes more likely to be represented in diabetic samples, and Augur sensitivity analysis to determine cell types or subtypes highly indicative of someone with diabetes.

As illustrated in Figure 15, the DE analysis between control and test groups identified upregulation of genes such as FCGBP (FDR = 1.12E-09), CD74 (FDR = 2.71E-06), HLA-B (FDR = 7.12E-05), HLA-E (FDR = 1.08E-04), HMOX2 (FDR = 7.01E-04), G6PD (FDR = 1.65E-03), and COL1A2 (FDR

= 8.38E-04). Downregulation of genes such as HSPA1B (FDR = 4.16E-12), HSPH1 (FDR = 1.03E-08), SLC6A6 (FDR = 8.27E-04), and DDIT3 (FDR = 8.30E-04) were detected.

The OR analysis heatmap (Figure 14B) presents retinal cell type proportions across three conditions: DM, DR, and nonDM. Key findings include notably reduced proportions of ACs, horizontal cells, and RGCs in DM but elevated in DR. Cones show higher proportions in nonDM subjects, while rods and MGCs remain relatively stable across each group. Astrocytes exhibit subtle changes, with slightly lower proportions in DM and higher in DR.

Discussion

Our study presents the first comprehensive single-cell transcriptomic atlas explicitly focusing on and demonstrating the critical importance of using fresh, living human retinal tissue. Using living samples provides a more accurate representation of *in vivo* transcriptional states compared to previous studies reliant on frozen or preserved tissue [13]. This approach has allowed us to capture subtle transcriptional changes and identify novel cell states that may have been overlooked in earlier studies using preserved tissues.

A key finding of our study is the discovery of a new cone photoreceptor subtype, ELF1-Cone, representing a significant advancement in our understanding of retinal cellular diversity. ELF1-Cones exhibit a unique transcriptional profile characterized by the expression of genes such as ASIC2, MSR1, and FRMD4A, suggesting multifaceted roles in pH sensing, neuroprotection, and cellular organization. Gene set enrichment analyses reveal that ELF1-Cones possess high energy production capacity, active protein synthesis machinery, and enhanced cell signaling capabilities, indicating their potential for rapid responses to changing retinal conditions.

The identification of ELF1 and PRKAA1 as key transcription factors provides insight into the regulatory mechanisms underlying ELF1-Cones' unique properties. The interplay between these transcription factors may coordinate the balance between energy production, environmental sensing, and neuroprotection that characterizes ELF1-Cones. Our dynamo analysis revealed a clear developmental trajectory from mlCone to ELF1-Cone, particularly evident in living samples. This trajectory suggests that ELF1-Cones represent a distinct stage in cone photoreceptor development. The cellular dynamics of ELF1-Cones, characterized by lower divergence and curvature, accompanied with moderate velocity and acceleration, indicate a more stable state compared to mlCone precursors. However, it still undergoes some degree of maturation or functional specialization.

CellOracle simulations further demonstrated the key roles of ELF1 and PRKAA1 in maintaining ELF1-Cone identity and guiding the developmental trajectory. These findings are consistent with previous studies showing that photoreceptors undergo a terminal differentiation phase where they acquire mature characteristics. In this process, different TFs are involved in the early formation and late function and maintenance of photoreceptors [49]. The differentiation of ELF1-Cone cells involves complex interactions between transcriptional regulation and metabolic remodeling. Our analyses suggest that ELF1 coordinates specific transcriptional programs critical for ELF1-Cone identity, while PRKAA1 may mediate important metabolic changes. This dual regulatory mechanism is consistent with recent findings on bidirectional interactions between transcriptional control and metabolic regulation in neuronal differentiation [50]. Importantly, our cell interaction analysis reveals that ELF1-Cone cells are not isolated entities but are integrated into a complex network of retinal cells.

Our study underscores the importance of using living human retinal tissue for accurate cellular mapping and trajectory inference. Living samples showed a clear, directional flow from mlCone to

ELF1-Cone, indicating an active differentiation pathway. In contrast, postmortem samples exhibited a disorganized, less directional pattern. The significant differences observed between living and postmortem samples in Dynamo analyses suggest that postmortem changes could affect the cellular patterns of the retina, potentially leading to misinterpretation of functional relationships. Postmortem changes, including ATP depletion, ion concentration shifts, enzyme activation, and RNA degradation, all have the possibility to affect cell state, gene expression, and observed developmental trajectories. While previous studies used adult retinal specimens removed of death and dissected within few hours [51], our results indicate that even these relatively short postmortem intervals can lead to significant alterations in cell trajectory. The disruptions observed in postmortem samples may obscure important nuances, particularly when studying subtle cellular transitions or newly identified cell types like ELF1-Cone. The sensitivity of ELF1-Cone cells to tissue degradation, evidenced by the loss of distinct differentiation flows in postmortem samples, suggests that these cells require active cellular processes to maintain their identity. This sensitivity could potentially make ELF1-Cones early indicators of retinal stress or disease.

We also identified three distinct GABAergic AC clusters (GABA-AC1, GABA-AC2, and GABA-AC3), alongside glycinergic ACs and an intermediate population, each with specialized functions. These distinct functional profiles advance our understanding of how different AC subtypes contribute to specific aspects of visual processing and retinal function.

Furthermore, the discovery of a potential corneal ulcer-associated cluster highlights the importance of considering the potential confounding effect from the underlying pathological conditions and the interconnectedness of both ocular and systemic health when considering the implications for gene expression and implicated disease pathways [52, 53].

In this study, we also addressed the challenges in differentiating between ACs, horizontal cells, and RGCs in scRNA-seq retinal samples, which commonly arise given their shared developmental trajectory and similar transcriptional profiles. All three cell types are derived from a common pool of retinal progenitor cells, and previous research in murine models has shown that genes associated with RGCs, ACs, and horizontal cells are expressed in a highly overlapping fashion in Atoh7-null retinas. Our study addresses these challenges through careful analysis and annotation, providing a more nuanced understanding of these closely related cell types.

Comparative analysis between nonDM, DM, and DR groups revealed significant differences in single-cell RNA profile patterns across cell types after excluding samples with markedly abnormal cell composition (with rod proportion less than 55%). Importantly, the differences in retinal cell type composition detected did not differ significantly between DM and nonDM samples. This suggests that early retinal neurodegeneration commonly associated with diabetes, damage to blood vessels, and structural changes are somewhat limited in the absence of DR. This finding is consistent with the understanding that detection of early diabetic lesions often requires advanced imaging techniques [54, 55]. Another noteworthy finding included the detection of a significant increase in the proportion of RGCs in the DR samples, particularly in Donor 4, contrary to the typical decrease expected in association with DR. We hypothesize this unexpected increase may be due to DR-induced stress and activation of RGCs, which alters their gene expression profiles and improves their detectability in scRNA-seq [56]. The difference in the increase in the proportion of RGCs in the DR samples may represent variation in the rate of progression among patients with diabetic retinopathy.

We also find the upregulation of inflammation-related genes (CD74, BTN3A2, HLA-B, HLA-E), complex alterations in stress response mechanisms (downregulation of HSPA1B, HSPH1; upregulation

of HMOX2), and changes in neurotransmitter signaling and metabolic pathways. These results support the growing recognition of DR as an inflammatory disease and suggest potential targets for therapeutic interventions [57]. While these findings provide valuable insights into DR pathogenesis, the primary objective of this investigation was to generate new human retina atlases, and an ongoing collection of more diabetic samples is underway for future analysis.

Our study encompasses a diverse range of samples, including those from diabetic and non-diabetic individuals, and both ante-mortem and post-mortem fresh samples. This diversity provided high-quality reference datasets for future research.

Despite the comprehensive nature of our study, we acknowledge some limitations including the use of samples from different disease status due to the challenges in obtaining living human retinal samples. This constraint highlights the need for collaborative efforts in the field to overcome the challenges of sample acquisition, an issue previously highlighted [58]. Moreover, the clinical reasons necessitating eye enucleation as outlined in Table 1, which includes conditions such as corneal staphyloma, ocular atrophy, corneal ulceration, and corneal perforation may potentially influence cell type distribution and gene expression profiles, representing an additional limitation of this study.

In conclusion, our study provides the atlas of fresh human retinal samples, significantly advancing our understanding of retinal cell diversity and function. This atlas serves as a valuable resource for the research community, paving the way for new discoveries in retinal biology and potential therapeutic interventions for retinal diseases, particularly diabetic retinopathy. Future research should elucidate ELF1-Cone functions, explore their role in retinal pathology, and leverage this atlas for potential therapeutic interventions.

Statements and Declarations

Data availability

Access to the scRNA-seq data generated is possible upon reasonable request.

Author information

Authors and Affiliations

Nottingham Ningbo China Beacons of Excellence Research and Innovation Institute, University of Nottingham Ningbo China, Ningbo, China, 315100

Luning Yang, Yiwen Ta, Qi Pan, Tengda Cai, Weihua Meng

Department of Ophthalmology, Lihuili Hospital affiliated with Ningbo University, Ningbo, China, 315040

Yunyan Ye

Department of Cardiology, Lihuili Hospital affiliated with Ningbo University, Ningbo, China, 315040

Jianhui Liu

Ningbo Institute of Innovation for Combined Medicine and Engineering, The Affiliated Li Huili Hospital, Ningbo University, Ningbo, China, 315201

Yang Zhou

Department of Ophthalmology, The Affiliated Ningbo Eye Hospital of Wenzhou Medical University, Ningbo, China, 315040

Yongqing Shao

PAPRSB Institute of Health Sciences, Universiti Brunei Darussalam, Bandar Seri, Begawan, BE1410, Brunei Darussalam

Zen Haut Lu, Lie Chen

Centre for Public Health, Institute of Clinical Science, Queen's University Belfast, Block B, Royal Hospital, Grosvenor Road, Belfast, Northern Ireland, BT12 6BA

Gareth McKay

School of Mathematical Sciences, University of Nottingham Ningbo China, Ningbo, China, 315100

Richard Rankin

Authors' Contributions

LY drafted the paper and performed the analysis. YT, QP, TC contributed to data formatting and correction. YY, JL, YZ, YS, QY, ZL, LC, GM, and RR provided comments on the paper. WM organized the project and provided comments.

Acknowledgment

This study was mainly funded by the Pioneer and Leading Goose R&D Program of Zhejiang Province 2023 with reference number 2023C04049 and Ningbo International Collaboration Program 2023 with reference number 2023H025.

Corresponding authors

Correspondence to Weihua Meng

Consent to Publish

All authors have consent for publication.

Conflict of Interest

The authors have no conflicts of interest to disclose.

Ethics approval

This study was approved by the Ethics Committee of the University of Nottingham Ningbo China; The Lihuili Hospital affiliated with Ningbo University; The Affiliated Ningbo Eye Hospital of Wenzhou Medical University.

References

1. Masland RH: **The neuronal organization of the retina**. *Neuron* 2012, **76**(2):266-280.
2. Hussey KA, Hadyniak SE, Johnston Jr RJ: **Patterning and development of photoreceptors in the human retina**. *Frontiers in cell and developmental biology* 2022, **10**:878350.
3. Grünert U, Martin PR: **Cell types and cell circuits in human and non-human primate retina**. *Progress in retinal and eye research* 2020, **78**:100844.
4. Sanes JR, Masland RH: **The types of retinal ganglion cells: current status and implications for neuronal classification**. *Annual review of neuroscience* 2015, **38**(1):221-246.
5. Lagnado L, Schmitz F: **Ribbon synapses and visual processing in the retina**. *Annual review of vision science* 2015, **1**(1):235-262.
6. Cen LP, Park KK, So KF: **Optic nerve diseases and regeneration: How far are we from the promised land?** *Clinical & experimental ophthalmology* 2023, **51**(6):627-641.
7. Voigt AP, Mulfaul K, Mullin NK, Flamme-Wiese MJ, Giacalone JC, Stone EM, Tucker BA, Scheetz TE, Mullins RF: **Single-cell transcriptomics of the human retinal pigment epithelium and choroid in health and macular degeneration**. *Proceedings of the National Academy of Sciences* 2019, **116**(48):24100-24107.
8. Chen K, Wang Y, Huang Y, Liu X, Tian X, Yang Y, Dong A: **Cross-species scRNA-seq reveals the cellular landscape of retina and early alterations in type 2 diabetes mice**. *Genomics* 2023, **115**(4):110644.
9. Lukowski SW, Lo CY, Sharov AA, Nguyen Q, Fang L, Hung SS, Zhu L, Zhang T, Grü

796 nert U, Nguyen T: **A single-cell transcriptome atlas of the adult human retina**. *The*
797 *EMBO journal* 2019, **38**(18):e100811.
798 10. Farjood F, Charniga C, Kiehl T, Stern J, Boles N: **Single-cell RNA sequencing reveals**
799 **the heterogeneity of the human retinal pigment epithelium**. *Investigative*
800 *Ophthalmology & Visual Science* 2020, **61**(7):3182-3182.
801 11. Voigt AP, Binkley E, Flamme-Wiese MJ, Zeng S, DeLuca AP, Scheetz TE, Tucker BA,
802 Mullins RF, Stone EM: **Single-cell RNA sequencing in human retinal degeneration**
803 **reveals distinct glial cell populations**. *Cells* 2020, **9**(2):438.
804 12. Wang J, Cheng X, Liang Q, Owen LA, Lu J, Zheng Y, Wang M, Chen S, DeAngelis
805 MM, Li Y: **Single-cell multiomics of the human retina reveals hierarchical transcription**
806 **factor collaboration in mediating cell type-specific effects of genetic variants on gene**
807 **regulation**. *Genome biology* 2023, **24**(1):269.
808 13. Liang Q, Cheng X, Wang J, Owen L, Shakoor A, Lillvis JL, Zhang C, Farkas M, Kim IK,
809 Li Y: **A multi-omics atlas of the human retina at single-cell resolution**. *Cell genomics*
810 2023, **3**(6).
811 14. Bakken TE, Hodge RD, Miller JA, Yao Z, Nguyen TN, Aevermann B, Barkan E,
812 Bertagnolli D, Casper T, Dee N: **Single-nucleus and single-cell transcriptomes**
813 **compared in matched cortical cell types**. *PloS one* 2018, **13**(12):e0209648.
814 15. Kropp M, Mohit M, Leroy-Ciocanea CI, Schwerm L, Harmening N, Bascuas T, De
815 Clerck E, Kreis AJ, Pajic B, Johnen S: **Mammalian Animal and Human Retinal Organ**
816 **Culture as Pre-Clinical Model to Evaluate Oxidative Stress and Antioxidant Intraocular**
817 **Therapeutics**. *Antioxidants* 2023, **12**(6):1211.

818 16. Kapp MB: **Ethical and legal issues in research involving human subjects: do you want**
819 **a piece of me?** *Journal of clinical pathology* 2006, **59**(4):335-339.
820 17. Lacar B, Linker SB, Jaeger BN, Krishnaswami SR, Barron JJ, Kelder MJ, Parylak SL,
821 Paquola AC, Venepally P, Novotny M: **Nuclear RNA-seq of single neurons reveals**
822 **molecular signatures of activation**. *Nature communications* 2016, **7**(1):11022.
823 18. Botling J, Edlund K, Segersten U, Tahmasebpoor S, Engström M, Sundström M,
824 Malmström P-U, Micke P: **Impact of thawing on RNA integrity and gene expression**
825 **analysis in fresh frozen tissue**. *Diagnostic Molecular Pathology* 2009, **18**(1):44-52.
826 19. Thakral S, Purohit P, Mishra R, Gupta V, Setia P: **The impact of RNA stability and**
827 **degradation in different tissues to the determination of post-mortem interval: A**
828 **systematic review**. *Forensic Science International* 2023:111772.
829 20. You M, Rong R, Zeng Z, Li H, Xia X, Ji D: **Single-cell RNA sequencing: A new**
830 **opportunity for retinal research**. *Wiley Interdisciplinary Reviews: RNA* 2021,
831 **12**(5):e1652.
832 21. Weir K, Leavey P, Santiago C, Blackshaw S: **Multiplexed analysis of retinal gene**
833 **expression and chromatin accessibility using scrna-seq and scatac-seq**. *JoVE*
834 *(Journal of Visualized Experiments)* 2021(169):e62239.
835 22. Wang Y, Yang X, Zhang Y, Hong L, Xie Z, Jiang W, Chen L, Xiong K, Yang S, Lin M:
836 **Single-cell RNA sequencing reveals roles of unique retinal microglia types in early**
837 **diabetic retinopathy**. *Diabetology & Metabolic Syndrome* 2024, **16**(1):49.
838 23. Hu Z, Mao X, Chen M, Wu X, Zhu T, Liu Y, Zhang Z, Fan W, Xie P, Yuan S: **Single-cell**
839 **transcriptomics reveals novel role of microglia in fibrovascular membrane of**

840 **proliferative diabetic retinopathy**. *Diabetes* 2022, **71**(4):762-773.

841 24. Hao Y, Hao S, Andersen-Nissen E, Mauck WM, Zheng S, Butler A, Lee MJ, Wilk AJ,
842 Darby C, Zager M: **Integrated analysis of multimodal single-cell data**. *Cell* 2021,
843 **184**(13):3573-3587. e3529.

844 25. Wolf FA, Angerer P, Theis FJ: **SCANPY: large-scale single-cell gene expression data**
845 **analysis**. *Genome biology* 2018, **19**:1-5.

846 26. Gayoso A, Lopez R, Xing G, Boyeau P, Valiollah Pour Amiri V, Hong J, Wu K,
847 Jayasuriya M, Mehlman E, Langevin M: **A Python library for probabilistic analysis of**
848 **single-cell omics data**. *Nature biotechnology* 2022, **40**(2):163-166.

849 27. Hänzelmann S, Castelo R, Guinney J: **GSVA: gene set variation analysis for**
850 **microarray and RNA-seq data**. *BMC bioinformatics* 2013, **14**:1-15.

851 28. La Manno G, Soldatov R, Zeisel A, Braun E, Hochgerner H, Petukhov V, Lidschreiber
852 K, Kastriti ME, Lönnerberg P, Furlan A: **RNA velocity of single cells**. *Nature* 2018,
853 **560**(7719):494-498.

854 29. Qiu X, Zhang Y, Martin-Rufino JD, Weng C, Hosseinzadeh S, Yang D, Pogson AN,
855 Hein MY, Min KHJ, Wang L: **Mapping transcriptomic vector fields of single cells**. *Cell*
856 2022, **185**(4):690-711. e645.

857 30. Kamimoto K, Stringa B, Hoffmann CM, Jindal K, Solnica-Krezel L, Morris SA:
858 **Dissecting cell identity via network inference and in silico gene perturbation**. *Nature*
859 2023, **614**(7949):742-751.

860 31. Jin S, Guerrero-Juarez CF, Zhang L, Chang I, Ramos R, Kuan C-H, Myung P, Plikus
861 MV, Nie Q: **Inference and analysis of cell-cell communication using CellChat**. *Nature*

862 *communications* 2021, **12**(1):1088.

863 32. Robinson MD, McCarthy DJ, Smyth GK: **edgeR: a Bioconductor package for**
864 **differential expression analysis of digital gene expression data**. *bioinformatics* 2010,
865 **26**(1):139-140.

866 33. Zheng L, Qin S, Si W, Wang A, Xing B, Gao R, Ren X, Wang L, Wu X, Zhang J:
867 **Pan-cancer single-cell landscape of tumor-infiltrating T cells**. *Science* 2021,
868 **374**(6574):abe6474.

869 34. Yan W, Peng Y, van Zyl T, Regev A, Shekhar K, Juric D, Sanes J: **Cell atlas of the**
870 **human fovea and peripheral retina. Sci Rep 10: 9802**. In.; 2020.

871 35. Wu F, Bard JE, Kann J, Yergeau D, Sapkota D, Ge Y, Hu Z, Wang J, Liu T, Mu X:
872 **Single cell transcriptomics reveals lineage trajectory of retinal ganglion cells in**
873 **wild-type and Atoh7-null retinas**. *Nature Communications* 2021, **12**(1):1465.

874 36. Li S, Mo Z, Yang X, Price SM, Shen MM, Xiang M: **Foxn4 controls the genesis of**
875 **amacrine and horizontal cells by retinal progenitors**. *Neuron* 2004, **43**(6):795-807.

876 37. Navneet S, Wilson K, Rohrer B: **Müller glial cells in the macula: their activation and**
877 **cell-cell interactions in age-related macular degeneration**. *Investigative*
878 *Ophthalmology & Visual Science* 2024, **65**(2):42-42.

879 38. Goldman D: **Müller glial cell reprogramming and retina regeneration**. *Nature Reviews*
880 *Neuroscience* 2014, **15**(7):431-442.

881 39. Luna G, Keeley PW, Reese BE, Linberg KA, Lewis GP, Fisher SK: **Astrocyte structural**
882 **reactivity and plasticity in models of retinal detachment**. *Experimental eye research*
883 2016, **150**:4-21.

884 40. Shekhar K, Lapan SW, Whitney IE, Tran NM, Macosko EZ, Kowalczyk M, Adiconis X,
885 Levin JZ, Nemesh J, Goldman M: **Comprehensive classification of retinal bipolar**
886 **neurons by single-cell transcriptomics**. *Cell* 2016, **166**(5):1308-1323. e1330.
887 41. van Wyk M, Pielecka-Fortuna J, Löwel S, Kleinlogel S: **Restoring the ON switch in**
888 **blind retinas: Opto-mGluR6, a next-generation, cell-tailored optogenetic tool**. *PLoS*
889 *biology* 2015, **13**(5):e1002143.
890 42. Puthussery T, Percival KA, Venkataramani S, Gayet-Primo J, Grünert U, Taylor WR:
891 **Kainate receptors mediate synaptic input to transient and sustained OFF visual**
892 **pathways in primate retina**. *Journal of Neuroscience* 2014, **34**(22):7611-7621.
893 43. Taylor WR, Smith RG: **Transmission of scotopic signals from the rod to rod-bipolar cell**
894 **in the mammalian retina**. *Vision research* 2004, **44**(28):3269-3276.
895 44. West ER, Lapan SW, Lee C, Kajderowicz KM, Li X, Cepko CL: **Spatiotemporal**
896 **patterns of neuronal subtype genesis suggest hierarchical development of retinal**
897 **diversity**. *Cell Reports* 2022, **38**(1).
898 45. Park SJ, Pottackal J, Ke J-B, Jun NY, Rahmani P, Kim I-J, Singer JH, Demb JB:
899 **Convergence and divergence of CRH amacrine cells in mouse retinal circuitry**. *Journal*
900 *of Neuroscience* 2018, **38**(15):3753-3766.
901 46. Poleg-Polsky A, Diamond JS: **Retinal circuitry balances contrast tuning of excitation**
902 **and inhibition to enable reliable computation of direction selectivity**. *Journal of*
903 *Neuroscience* 2016, **36**(21):5861-5876.
904 47. Schmidt BP, Boehm AE, Tuten WS, Roorda A: **Spatial summation of individual cones**
905 **in human color vision**. *PLoS One* 2019, **14**(7):e0211397.

906 48. Masri RA, Weltzien F, Purushothuman S, Lee SC, Martin PR, Grünert U: **Composition**
907 **of the inner nuclear layer in human retina**. *Investigative Ophthalmology & Visual*
908 *Science* 2021, **62**(9):22-22.
909 49. Demb JB, Singer JH: **Functional circuitry of the retina**. *Annual review of vision science*
910 2015, **1**(1):263-289.
911 50. Agathocleous M, Harris WA: **Metabolism in physiological cell proliferation and**
912 **differentiation**. *Trends in cell biology* 2013, **23**(10):484-492.
913 51. Lu Y, Shiau F, Yi W, Lu S, Wu Q, Pearson JD, Kallman A, Zhong S, Hoang T, Zuo Z:
914 **Single-cell analysis of human retina identifies evolutionarily conserved and**
915 **species-specific mechanisms controlling development**. *Developmental cell* 2020,
916 **53**(4):473-491. e479.
917 52. Kang Y, Zhang H, Hu M, Ma Y, Chen P, Zhao Z, Li J, Ye Y, Zheng M, Lou Y:
918 **Alterations in the ocular surface microbiome in traumatic corneal ulcer patients**.
919 *Investigative Ophthalmology & Visual Science* 2020, **61**(6):35-35.
920 53. Lobov I, Mikhailova N: **The role of Dll4/Notch signaling in normal and pathological**
921 **ocular angiogenesis: Dll4 controls blood vessel sprouting and vessel remodeling in**
922 **normal and pathological conditions**. *Journal of ophthalmology* 2018, **2018**(1):3565292.
923 54. Ferreira JT, Alves M, Dias-Santos A, Costa L, Santos BO, Cunha JP, Papoila AL,
924 Pinto LA: **Retinal neurodegeneration in diabetic patients without diabetic retinopathy**.
925 *Investigative ophthalmology & visual science* 2016, **57**(14):6455-6460.
926 55. Satue M, Cipres M, Melchor I, Gil-Arribas L, Vilades E, Garcia-Martin E: **Ability of**
927 **swept source OCT technology to detect neurodegeneration in patients with type 2**

928 **diabetes mellitus without diabetic retinopathy**. *Japanese Journal of Ophthalmology*
929 2020, **64**:367-377.
930 56. Wang Q, Qiao Z, Kang W, Zhu L, Zhang X: **Comparative analysis of co-culture and**
931 **monoculture models in simulating diabetic neurovascular dysfunction: insights into**
932 **diabetic retinopathy**. *Frontiers in Endocrinology* 2023, **14**:1215218.
933 57. Semeraro F, Morescalchi F, Cancarini A, Russo A, Rezzola S, Costagliola C: **Diabetic**
934 **retinopathy, a vascular and inflammatory disease: therapeutic implications**. *Diabetes*
935 *& metabolism* 2019, **45**(6):517-527.
936 58. Tran NM, Shekhar K, Whitney IE, Jacobi A, Benhar I, Hong G, Yan W, Adiconis X,
937 Arnold ME, Lee JM: **Single-cell profiles of retinal ganglion cells differing in resilience to**
938 **injury reveal neuroprotective genes**. *Neuron* 2019, **104**(6):1039-1055. e1012.
939
940

Figure legends

Fig1 Uniform manifold approximation and projection (UMAP) plot of single-cell RNA sequencing (scRNA-seq) data integrated from nine fresh human retinal samples, using the Leiden clustering algorithm at various resolutions, from 0.05 to 1.0. The clustering resolution of 0.3 was chosen as the best value. UMAP plots illustrate the evolution of cell clusters across increasing Leiden algorithm resolutions (leiden_0_05 to leiden_1_0) for integrated data from nine fresh human retinal samples. Each subplot represents a distinct resolution, with colored and numbered clusters indicating different cell populations. The last panel (ID) displays an integrated UMAP visualization where each color represents a different dataset from the nine fresh human retinal samples, highlighting the effectiveness of the integration method.

Fig2 Comprehensive analysis of human retinal major cell type annotation

(A) Uniform manifold approximation and projection (UMAP) plots of integrated human retina sample datasets, colored and labeled by major human retinal cell types.

(B) Dot plots summarizing the known markers used to identify major cell types and a selection of genes distinguishing each cluster for retinal samples. Each row corresponds to a specific major cell type, and the columns correspond to a list of key marker genes; brackets on the top of the plot detail the cell type identified by the genes.

(C) Scatter plot of different expressed genes (DEGs) for each major human retinal cell type. Genes of interest are labeled to indicate significant DE patterns based on up and low-regulated DEGs. Upregulated genes were defined as those with log fold change > 0.5, and downregulated genes as those with log fold change < -0.5.

Fig3 Comprehensive analysis of cell types and clusters in human retina.

(A) Circular representation of Uniform Manifold Approximation and Projection (UMAP) clustering of the integrated datasets of major cell types and the experimental condition compositions for each group.

(B) Stacked bar plot showing the distribution ratios of major cell types across the nine human retina samples.

(C) Stacked bar plot showing the distribution of bipolar cell subtypes within each sample, with cell types including BB-GB, CB1, DB2, DB3a, DB3b, DB4, DB5, DB6, FMB, IMB, OFFx, and RBC.

(D) Stacked bar plot showing the distribution of cone subtypes within each sample, with cell types including the Corneal Repair cluster (CR), mlCone, sCone, and ELF1-Cone.

(E) Stacked bar plot showing the distribution of AC subtypes within each sample, with cell types including GABA-AC1, GABA-AC2, GABA-AC3, gly-AC and intermediate-AC.

Fig4 Gene set variation analysis **(**GSVA) plots showing the terms of the hallmark gene set enrichment pathway for each identified major retina cell type. Each row represents a hallmark pathway, and each column corresponds to a major human retinal cell type. Pathways are annotated by their direction of regulation (up or down) and the significance of enrichment. The color scale indicates the significance level (p value) of enrichment, with darker red indicating higher significance.

Fig5 Comparative analysis of astrocytes (ACs), horizontal cells, and retinal ganglion cells (RGCs).

(A-C) Uniform manifold approximation and projection (UMAP) plots of the expression density for genes marking ACs, horizontal cells, and RGCs separately.

(D) Heatmap representing the expression levels of selected marker genes for identifying ACs, horizontal cells, and RGCs.

(E) Dot plots summarizing the selected marker for differentiation. Columns correspond to the three cell types; rows correspond to a list of key marker genes; brackets on the right side detail the cell type indicated by the genes.

(F) UMAP plot showing the clustering of retinal cell types based on gene expression profiles, highlighting AC, horizontal cell, and RGC populations. UMAP plots of the selected cluster, colored and labeled by amacrine cell, horizontal cell, and retinal ganglion cell annotations.

Fig6 Comparative analysis of astrocytes and müller glia cells (MGCs).

(A) Uniform manifold approximation and projection (UMAP) plot depicting the clustering of astrocytes and MGCs based on their gene expression profiles. Astrocytes are shown in blue and MGCs in orange.

(B) Heatmap (left) and dot plot (right) summarizing the expression levels of key marker genes in astrocytes and MGCs. Columns correspond to MGCs and astrocytes, and the rows correspond to a list of key marker genes, brackets on the right side detail the cell type that the genes identify.

Fig7 Characterization of bipolar cells (BCs) subtypes in the human retina.

(A) 12 subtypes of BCs are identified in this study. OFF subtypes (1, 2, 3a-3b, FMC, OFFx) hyperpolarize in response to light, while ON subtypes (RBC, 4, 5, 6, BB+GB, IMB) depolarize to the same stimuli. There are 11 types of cone BCs and one type of rod BCs.

(B) Uniform manifold approximation and projection (UMAP) plots of the expression density for specific marker genes across BC subtypes.

(C) Dot plots summarizing the known markers used to identify BC subtypes and a selection of genes distinguishing each BC cluster. Each row corresponds to a specific BC subtype, and the columns correspond to a list of key marker genes, brackets on the top of the plot detail the bipolar cell subtype

that these genes identify.

(D) UMAP plot showing the clustering of bipolar cell subtypes based on gene expression profiles, with each color representing a different BC subtype.

Fig8 Characterization of amacrine cell (AC) subtypes based on gene expression.

(A) Uniform manifold approximation and projection (UMAP) plot showing the clustering of different AC subtypes. The subtypes are color-coded: GABA-AC1 (blue), Intermediate-AC (orange), Gly-AC (green), GABA-AC2 (red), and GABA-AC3 (purple).

(B) Dot plot (top) and violin plot (bottom) summarizing the expression levels of key marker genes in five AC subtypes. Rows correspond to each subtype, and the columns correspond to a list of key marker genes, brackets on the top detail the cell type that these genes identify.

(C) Gene Ontology (GO) analysis of GABA-AC1, GABA-AC2, and GABA-AC3 sub cell types. In this panel, the top 10 enriched GO terms are shown for each category, and these terms are sorted based on gene count. The bars represent the number of genes involved in each GO term, with the total gene count displayed at the right of each bar. Bar plots are split into three sections in terms of molecular function (MF, purple), cellular component (CC, blue), and biological process (BP, green).

(D) The dot plot illustrates the results of GO enrichment analysis for differentially expressed genes in various amacrine cell subtypes (GABA-AC1, GABA-AC2, GABA-AC3, Gly-AC, and Intermediate-AC). The top 10 most significant GO terms are displayed for each cluster based on adjusted p-value, ensuring that the most statistically significant terms are highlighted. The y-axis displays the top 10 significantly enriched GO terms for each cell subtype, encompassing biological processes, cellular components, and molecular functions. The x-axis represents the different amacrine cell subtypes. Each dot's size corresponds to the gene count, while the color intensity indicates the gene

ratio. The color scale ranges from yellow (lower gene ratio) to purple (higher gene ratio).

Fig9 Gene expression analysis and clustering of cone subtypes in retinal cells.

(A) Uniform manifold approximation and projection (UMAP) plots of the expression density for specific marker genes across cone cell sub-clusters.

(B) Dot plots summarizing the known markers used to identify each cone cell sub-cluster and a selection of genes distinguishing each cone cell cluster. Each row corresponds to a specific cone subtype or specific cluster, and the columns correspond to a list of key marker genes, brackets on the top of the plot detail the cluster that these genes identify. Subclusters include corneal repair related cluster (CR), mlCone, sCone, and ELF1-Cone. The size of the dots represents the fraction of cells in each group, and the color intensity represents the mean expression level.

(C) UMAP plot illustrating the clustering of cone based on gene expression profiles, with each color representing a different subtype or cluster: CR (blue), mlCone (orange), ELF1-Cone (green), and sCone (red).

Fig10 Multi-omics analysis of cellular heterogeneity and gene expression patterns in cones.

(A) Heatmap representing expression levels of top ten differentially expressed genes across individual cone photoreceptors. Rows correspond to marker genes, columns to individual cells, and colors indicate expression intensity (red: high, blue: low). The color bar at the top denotes cell types, including corneal repair related cluster (CR), mlCone, ELF1-Cone, and sCone.

(B) Gene Ontology (GO) analysis for the ELF1-Cone cluster. The bar plot displays enriched GO terms categorized by biological processes (BP), cellular components (CC), and molecular functions (MF). The x-axis represents gene count in each pathway, and the y-axis lists specific GO terms.

(C) GSVA (Gene Set Variation Analysis) heatmap showing enrichment scores for hallmark gene sets across different cone cell clusters. Red indicates the positive enrichment, and blue indicates the negative enrichment. The top and left-side brackets are the results of hierarchical clustering of both cone cell types and enrichment pathways.

(D) Correlation heatmap of regulon modules in cone photoreceptors, highlighting patterns of co-expression. Four distinct modules are numbered and annotated. Key regulons with the highest residual sum of squares (RSS) rank values, identified by SCENIC analysis, are labeled on the right hand side.

(E) UMAP (Uniform Manifold Approximation and Projection) plots showing the gene expression distribution of regulons from the four identified modules (M1-M4) across all cone populations.

(F) RSS rank plot of active regulon in the cluster of ELF1-Cone. The x-axis represents the rank of each regulon, and the y-axis shows the RSS scores.

Fig11 Dynamo and CellOracle analysis of ELF1-Cone differentiation and regulation in human retina

(A) UMAP plots showing cell type distributions and velocity vectors across all datasets, living datasets, and cadaveric datasets. Cell types are color that: coreal repair related cluster (red), mlCone (pink), ELF1-Cone (light red), and sCone (blue). Arrows indicate predicted cell state transitions.

(B) Cellular dynamics analysis of living datasets, showing speed, divergence, acceleration, and curvature. Color scales indicate relative values for each metric.

(C) CellOracle perturbation simulations comparing living Datasets (left) with ELF1 knock out (middle) and PRKAA1 knock out (right). Arrows represent predicted cell state transitions under each condition.

Fig12 CellChat analysis showing cell-cell interactions between different cone subtypes. The circular chord diagram illustrates signaling pathways and interaction strengths between cell types, with a focus on ELF1-Cone interactions.

Fig13 Analysis of gene expression in horizontal cell subtypes.

(A) Uniform manifold approximation and projection (UMAP) plots showing the expression of LHX1 and ISL1 genes across horizontal cell subtypes. The color scale indicates the expression level of each gene.

(B) Dot plot summarizing the expression levels of key marker genes in H1 and H2 horizontal cell subtypes. Rows correspond to H1 and H2, and the columns correspond to a list of key marker genes, brackets on the top detail the horizontal cell subtype that these genes identify.

(C) UMAP plot depicting the clustering of horizontal cell subtypes based on gene expression profiles, with H1 cells shown in blue and H2 cells in orange.

Fig14 Comparative analysis of retinal cell types of diabetic conditions

(A) Boxplots depicting the proportion of cell classes across three conditions: diabetic (DM), diabetic retinopathy (DR), and non-diabetic (nonDM). The plots show the distribution of various retinal cell types, including astrocyte, horizontal, retinal ganglion cell (RGC), T cell (TC), rod, bipolar cell, amacrine, cone, microglia, and müller glia cells (MGC).

(B) Heatmap of odds ratio (OR) analysis showing differences in cell abundance between major human retinal cell types between groups (DR, DM, and nonDM). A p value was calculated by one-sided Fisher's exact test and corrected by Benjamini-Hochberg procedure. OR > 1.5 and adjusted p value (Padj) < 0.05 indicating that this subpopulation was more likely to be associated

with this immune subtype, whereas OR < 0.5 and adjusted p value < 0.05 indicated that it was less likely to be commonly associated with this retinal cell type.

Fig15 Volcano plot showing the results of differential expression (DE) between test group (diabetes, diabetic retinopathy) and control group (non-diabetes) in human retina samples. The plot illustrates the distribution of genes based on their expression changes, with the x-axis representing log2 fold change and the y-axis showing -log10 p-value. Colored dots represent different categories of genes: grey for not statistically different (NS), green for genes meeting the log2 fold change threshold, blue for genes meeting the p-value threshold, and red for genes meeting both thresholds. Key genes of interest are labeled with arrows for easy identification. The horizontal dashed line indicates the p-value threshold for statistically meaningful differences, while vertical dashed lines denote the log2 fold change thresholds for biologically relevant expression changes.

Table 1. Retinal sample details

Donor	Treatment	Eye	Sex	Age	Diabetic Status	Eye Removal Reasons	Hospital
01	fresh/living	left	Male	76	DM	Corneal staphyloma	L.H.
02	fresh/living	left	Male	55	nonDM	Eyeball atrophy	L.H.
03	fresh/cadaveric	both eyes	Female	55	DM	SCT-H-PON	Y.H.
04	fresh/cadaveric	both eyes	Male	55	DR	BSH	Y.H.
05	fresh/living	right	Male	71	nonDM	Corneal ulcer	Y.H.
06	fresh/living	left	Female	50	nonDM	Eyeball atrophy	Y.H.
07	fresh/living	right	Female	68	nonDM	Corneal perforation	Y.H.

Fresh/living: Fresh retina samples collected from living humans without freezing. Fresh/cadaveric: Fresh retina samples collected from recently deceased bodies without freezing. DM: Samples with diabetes. DR: Samples with diabetic retinopathy. nonDM: Samples without diabetes. SCT-H-PON: Severe craniocerebral trauma with hemorrhage in the periphery of the optic nerve. BSH: Brain stem hemorrhage. L.H.: The Affiliated Li Huili Hospital. Y.H.: The Affiliated Ningbo Eye Hospital of Wenzhou Medical University.

Table 2. Counts and proportion of major cell types in each human retinal scRNA-seq datasets. The major cell classes include amacrine cells, astrocytes, bipolar cells,

Donor	Diabetic Status	Amacrine	Astrocyte	Bipolar	Cone	RGC	Horizontal	Microglia	MGC	Rod	T cell

cones, retinal ganglion cells (RGCs), horizontal cells, microglia, müller glia cells (MGCs), rods and T cells.

01	DM	90 (0.62%)	76 (0.53%)	2667 (18.49%)	403 (2.79%)	0	148 (1.03%)	3252 (22.55%)	905 (6.27%)	6167 (42.76%)	715 (4.96%)
02	nonDM	9 (0.09%)	1 (0.01%)	528 (5.47%)	9 (0.09%)	0	9 (0.09%)	141 (1.46%)	136 (1.41%)	8732 (90.53%)	80 (0.83%)
03	DM	2 (0.01%)	5 (0.03%)	681 (4.88%)	336 (2.41%)	2 (0.01%)	13 (0.09%)	36 (0.26%)	1347 (9.65%)	11533 (82.60%)	8 (0.06%)
03	DM	25 (0.15%)	19 (0.13%)	753 (4.67%)	507 (3.14%)	0	12 (0.07%)	42 (0.26%)	1923 (11.92%)	12850 (79.62%)	8 (0.05%)
04	DR	310 (1.66%)	23 (0.16%)	1345 (7.22%)	150 (0.81%)	102 (0.55%)	105 (0.56%)	226 (1.21%)	1386 (7.44%)	14972 (80.37%)	11 (0.06%)
04	DR	88 (0.64%)	14 (0.10%)	424 (3.10%)	140 (1.02%)	22 (0.16%)	23 (0.17%)	211 (1.54%)	917 (6.71%)	11815 (86.46%)	12 (0.09%)
05	nonDM	24 (0.29%)	14 (0.10%)	45 (0.55%)	312 (3.80%)	0	1 (0.01%)	84 (1.02%)	893 (10.87%)	6788 (82.66%)	51 (0.62%)
06	nonDM	44 (0.72%)	15 (0.10%)	1421 (23.24%)	165 (2.70%)	1 (0.02%)	75 (1.23%)	216 (3.53%)	855 (13.98%)	3207 (52.45%)	115 (1.88%)
07	nonDM	129 (2.14%)	145 (1.01%)	623 (10.32%)	156 (2.58%)	8 (0.13%)	119 (1.97%)	829 (13.73%)	1582 (26.21%)	2424 (40.15%)	22 (0.36%)

DM: Samples with diabetes. DR: Samples with diabetic retinopathy. nonDM: Samples without diabetes.

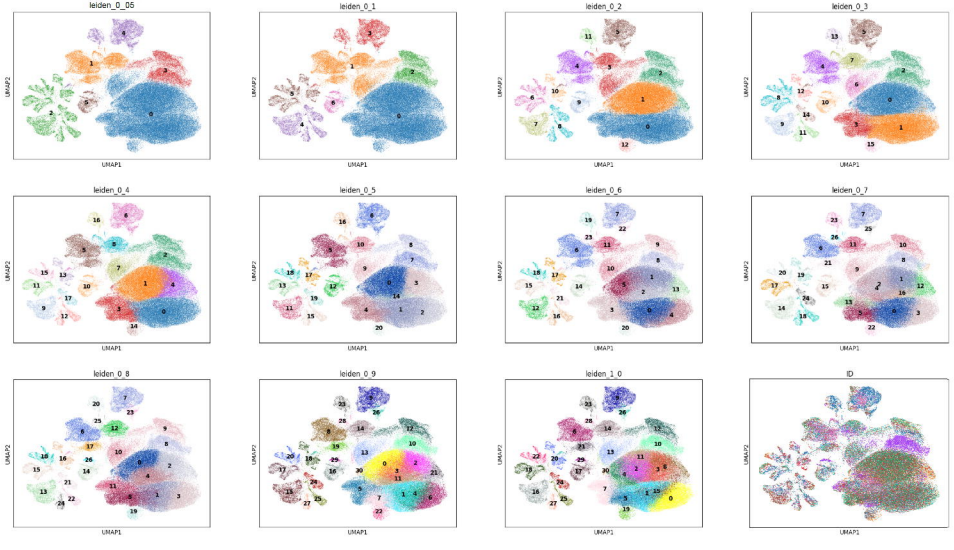
leiden_0_05
leiden_0_1
leiden_0_2
leiden_0_3
leiden_0_4
leiden_0_5
leiden_0_6
leiden_0_7
leiden_0_8
leiden_0_9
leiden_1_0
ID
UMAP1
UMAP2

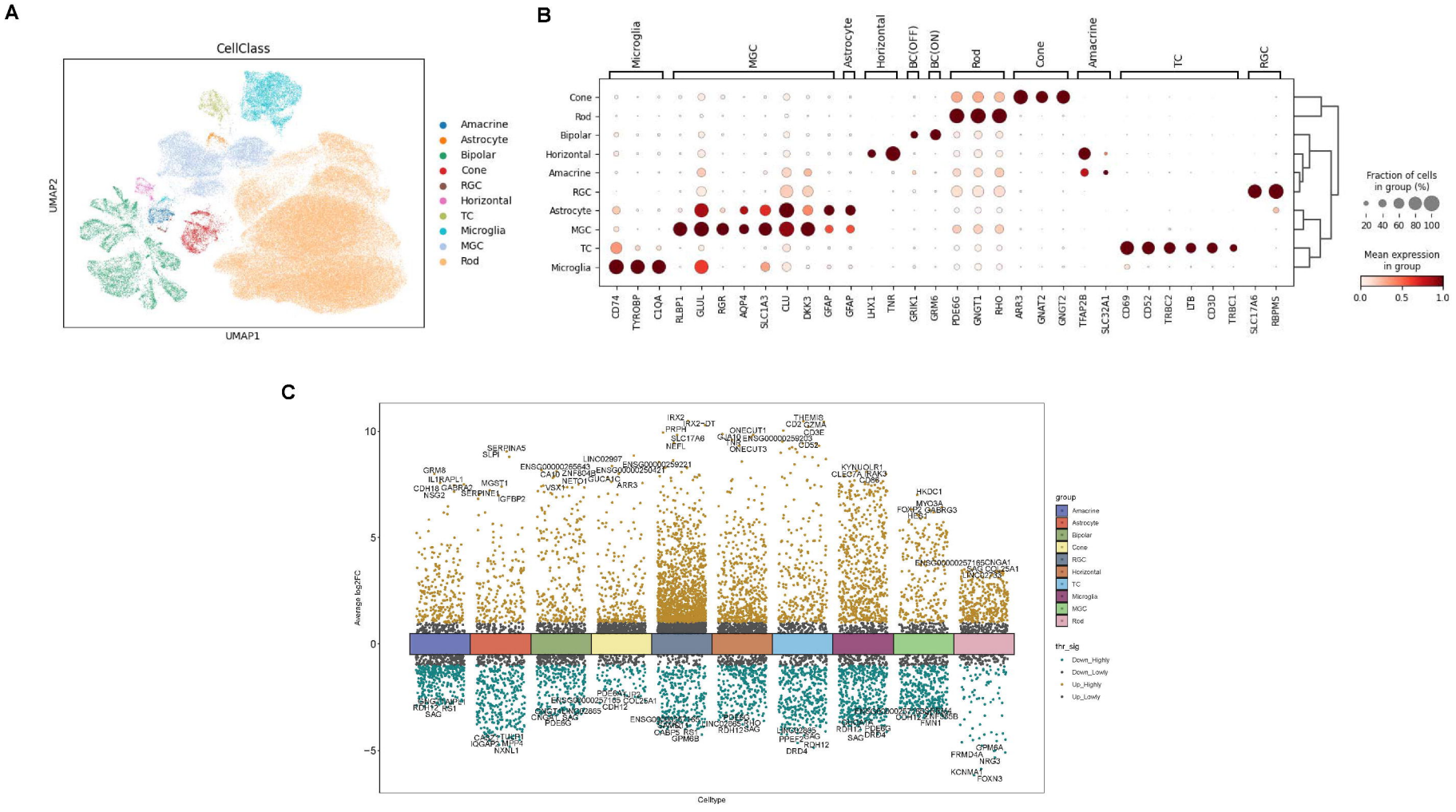
A
CellClass
UMAP2
UMAP1
Amacrine
Astrocyte
Bipolar
Cone
RGC
Horizontal
TC
Microglia
MGC
Rod
B
Microglia
MGC
Astrocyte
Horizontal
BC(OFF)
BC(ON)
Rod
Cone
Amacrine
TC
RGC
Cone
Rod
Bipolar
Horizontal
Amacrine
RGC
Astrocyte
MGC
TC
Microglia
CD74
TYROBP
C1QA
RLBP1
GULL
RGR
AQP4
SLC1A3
CLU
DKK3
GFAP
GFAP
LHX1
TNR
GRIK1
GRM6
PDE6G
GNGT1
RHO
ARR3
GNAT2
GNGT2
TFAP2B
SLC32A1
CD69
CD52
TRBC2
LTB
CD3D
TRBC1
SLC17A6
RBPMS
Fraction of cells in group (%)
20 40 60 80 100
Mean expression in group
0.0 0.5 1.0
C
Average log2FC
10
5
0
−5
Celltype
group
Amacrine
Astrocyte
Bipolar
Cone
RGC
Horizontal
TC
Microglia
MGC
Rod
thr_sig
Down_Highly
Down_Lowly
Up_Highly
Up_Lowly

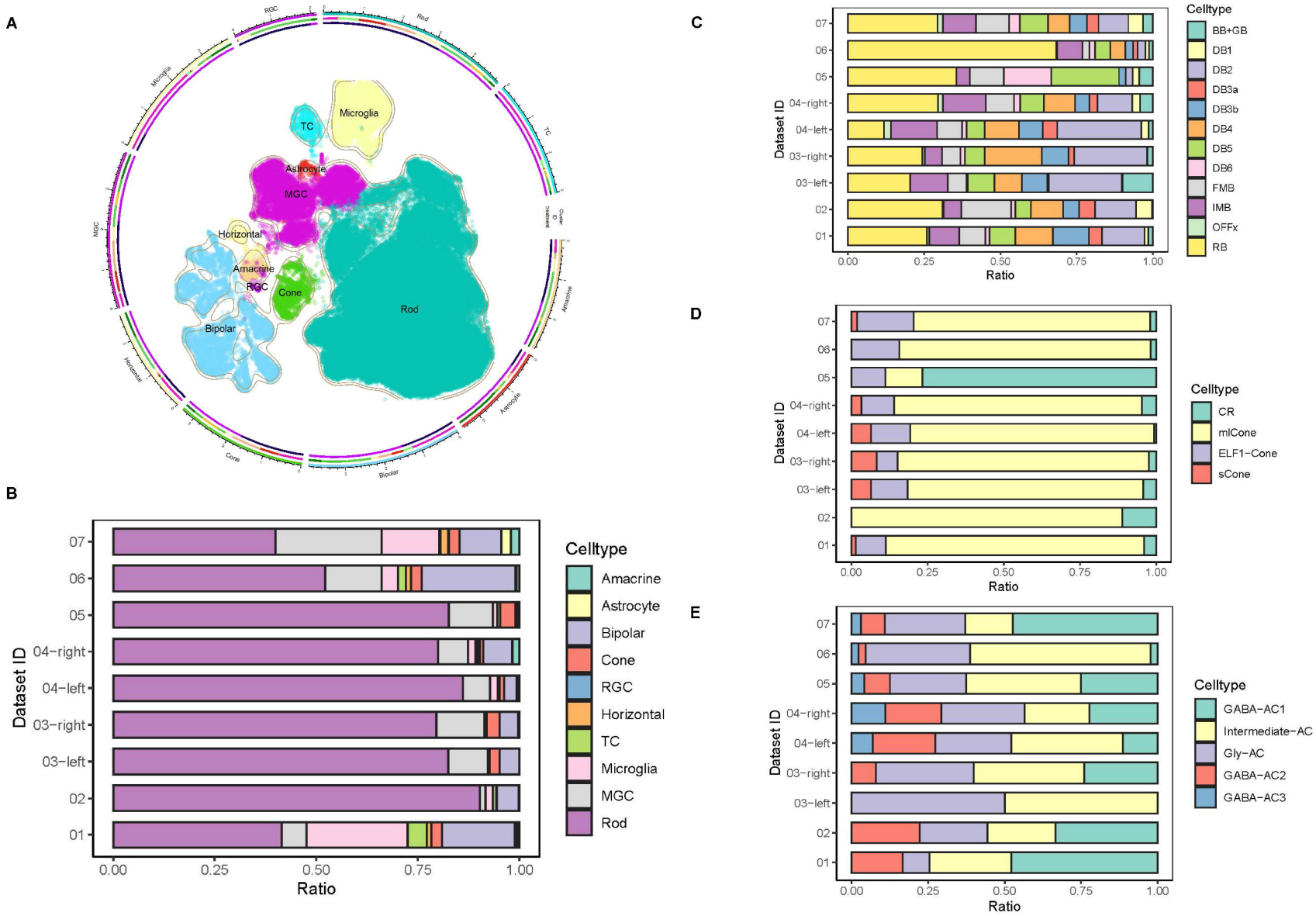
A
Microglia
TC
Astrocyte
MGC
Horizontal
Amacrine
RGC
Cone
Bipolar
Rod
B
Dataset ID
07
06
05
04−right
04−left
03−right
03−left
02
01
0.00
0.25
0.50
0.75
1.00
Ratio
Celltype
Amacrine
Astrocyte
Bipolar
Cone
RGC
Horizontal
TC
Microglia
MGC
Rod
C
Celltype
BB+GB
DB1
DB2
DB3a
DB3b
DB4
DB5
DB6
FMB
IMB
OFFx
RB
D
Celltype
CR
mlCone
ELF1−Cone
sCone
E
Celltype
GABA−AC1
Intermediate−AC
Gly−AC
GABA−AC2
GABA−AC3

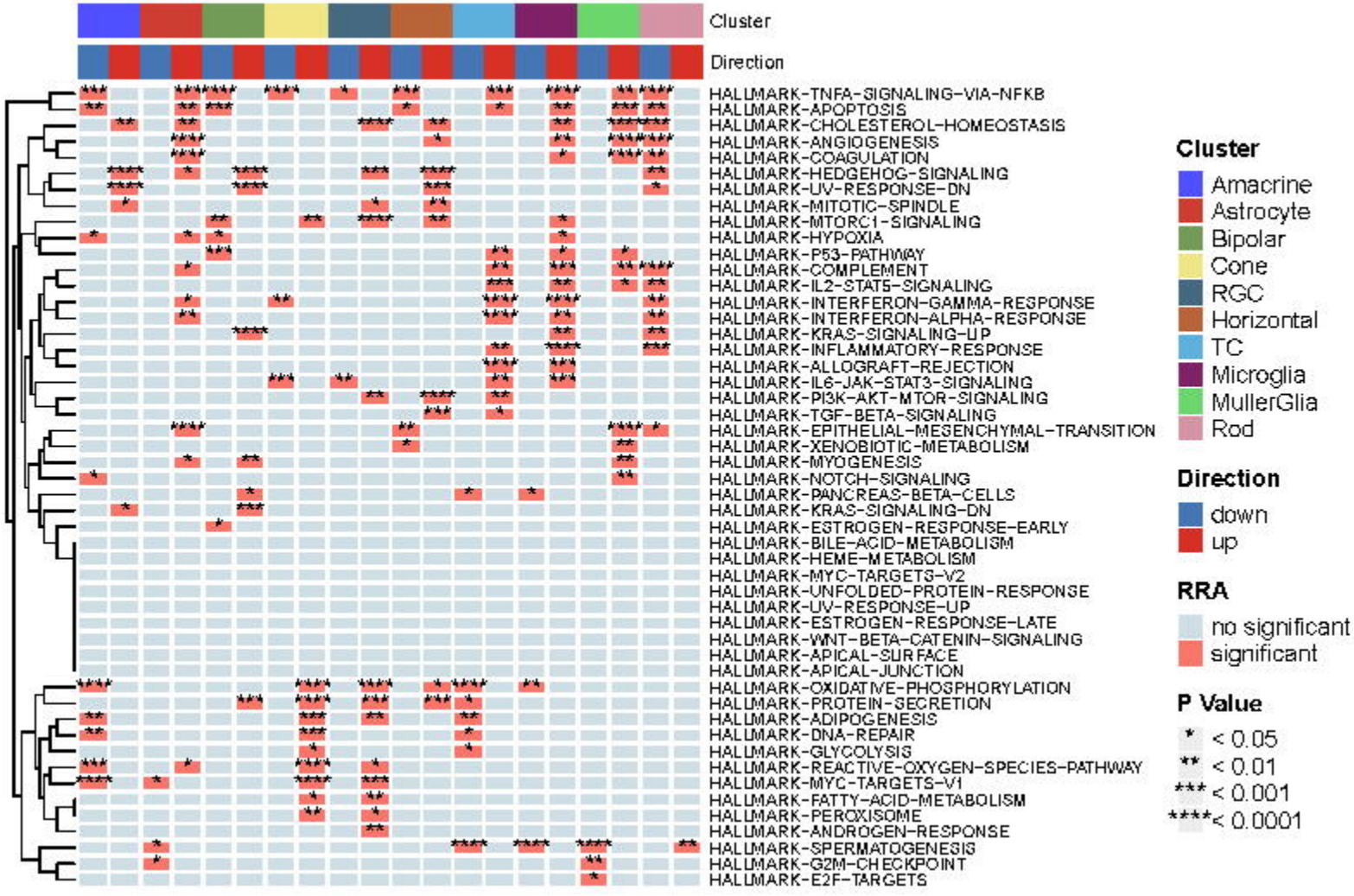
Cluster
Direction
HALLMARK-TNFA-SIGNALING-VIA-NFKB
HALLMARK-APOPTOSIS
HALLMARK-CHOLESTEROL-HOMEOSTASIS
HALLMARK-ANGIOGENESIS
HALLMARK-COAGULATION
HALLMARK-HEDGEHOG-SIGNALING
HALLMARK-UV-RESPONSE-DN
HALLMARK-MITOTIC-SPINDLE
HALLMARK-MTORC1-SIGNALING
HALLMARK-HYPOXIA
HALLMARK-P53-PATHWAY
HALLMARK-COMPLEMENT
HALLMARK-IL2-STAT5-SIGNALING
HALLMARK-INTERFERON-GAMMA-RESPONSE
HALLMARK-INTERFERON-ALPHA-RESPONSE
HALLMARK-KRAS-SIGNALING-UP
HALLMARK-INFLAMMATORY-RESPONSE
HALLMARK-ALLOGRAFT-REJECTION
HALLMARK-IL6-JAK-STAT3-SIGNALING
HALLMARK-PI3K-AKT-MTOR-SIGNALING
HALLMARK-TGF-BETA-SIGNALING
HALLMARK-EPITHELIAL-MESENCHYMAL-TRANSITION
HALLMARK-XENOBIOTIC-METABOLISM
HALLMARK-MYOGENESIS
HALLMARK-NOTCH-SIGNALING
HALLMARK-PANCREAS-BETA-CELLS
HALLMARK-KRAS-SIGNALING-DN
HALLMARK-ESTROGEN-RESPONSE-EARLY
HALLMARK-BILE-ACID-METABOLISM
HALLMARK-HEME-METABOLISM
HALLMARK-MYC-TARGETS-V2
HALLMARK-UNFOLDED-PROTEIN-RESPONSE
HALLMARK-UV-RESPONSE-UP
HALLMARK-ESTROGEN-RESPONSE-LATE
HALLMARK-WNT-BETA-CATENIN-SIGNALING
HALLMARK-APICAL-SURFACE
HALLMARK-APICAL-JUNCTION
HALLMARK-OXIDATIVE-PHOSPHORYLATION
HALLMARK-PROTEIN-SECRETION
HALLMARK-ADIPOGENESIS
HALLMARK-DNA-REPAIR
HALLMARK-GLYCOLYSIS
HALLMARK-REACTIVE-OXYGEN-SPECIES-PATHWAY
HALLMARK-MYC-TARGETS-V1
HALLMARK-FATTY-ACID-METABOLISM
HALLMARK-PEROXISOME
HALLMARK-ANDROGEN-RESPONSE
HALLMARK-SPERMATOGENESIS
HALLMARK-G2M-CHECKPOINT
HALLMARK-E2F-TARGETS
Cluster
Amacrine
Astrocyte
Bipolar
Cone
RGC
Horizontal
TC
Microglia
MullerGlia
Rod
Direction
down
up
RRA
no significant
significant
P Value
* < 0.05
** < 0.01
*** < 0.001
**** < 0.0001

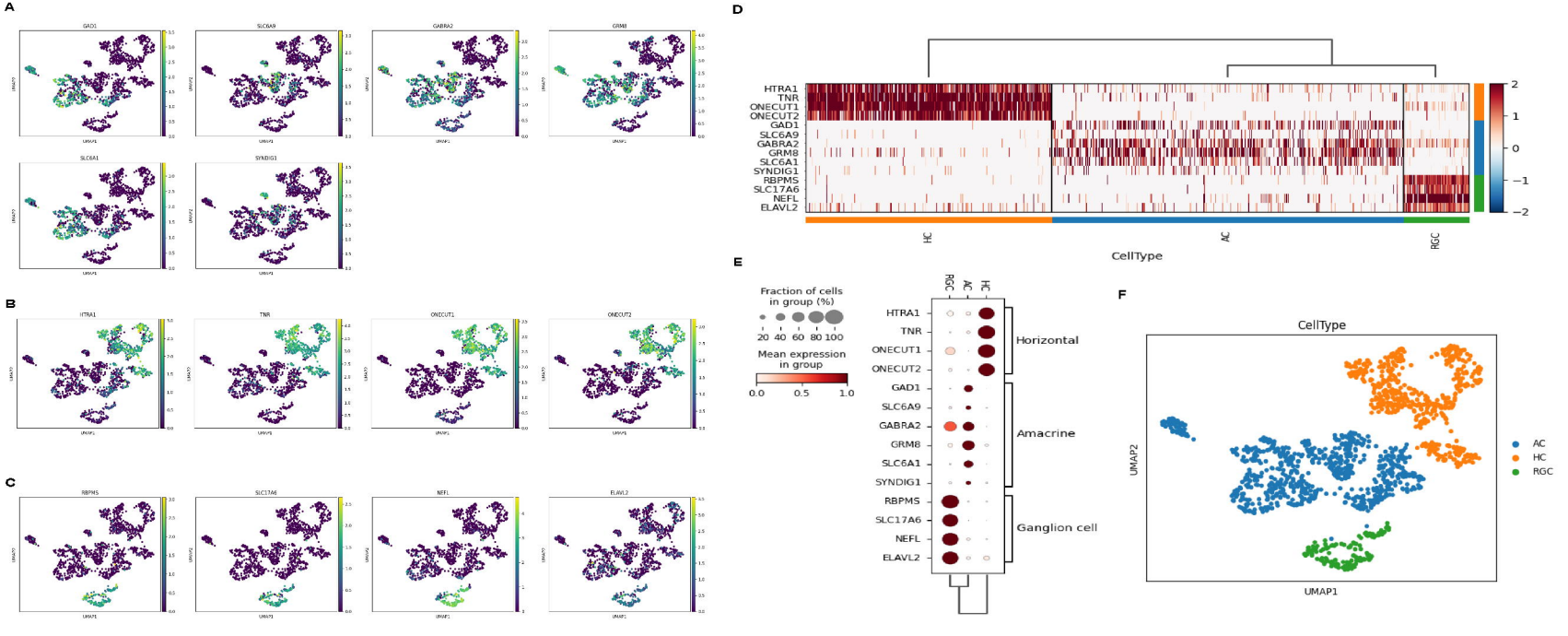
A
GAD1
SLC6A9
GABRA2
GRM8
SLC6A1
SYNDIG1
B
HTRA1
TNR
ONECUT1
ONECUT2
C
RBPMS
SLC17A6
NEFL
ELAVL2
D
HTRA1
TNR
ONECUT1
ONECUT2
GAD1
SLC6A9
GABRA2
GRM8
SLC6A1
SYNDIG1
RBPMS
SLC17A6
NEFL
ELAVL2
HC
AC
RGC
CellType
2
1
0
−1
−2
E
Fraction of cells in group (%)
20 40 60 80 100
Mean expression in group
0.0 0.5 1.0
RGC
AC
HC
Horizontal
Amacrine
Ganglion cell
F
CellType
UMAP2
UMAP1
AC
HC
RGC

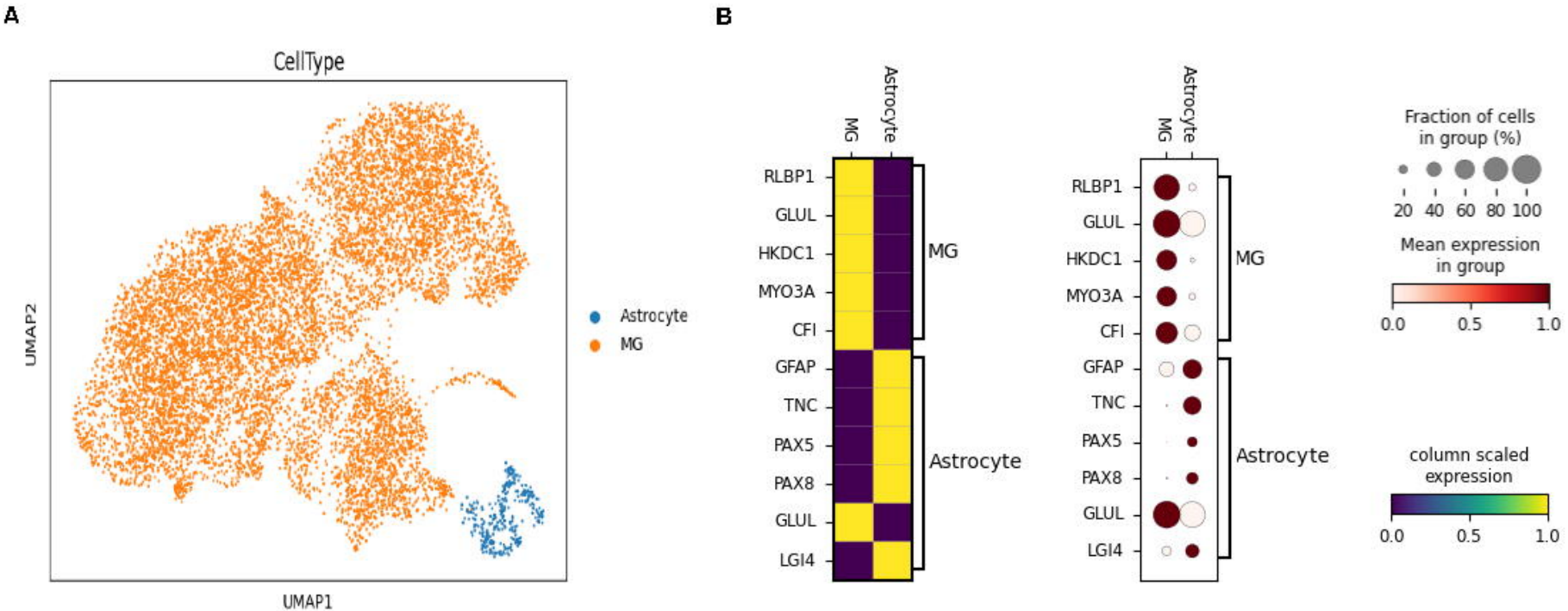
A
CellType
UMAP2
UMAP1
Astrocyte
MG
B
MG
Astrocyte
RLBP1
GLUL
HKDC1
MYO3A
CFI
GFAP
TNC
PAX5
PAX8
GLUL
LGI4
MG
Astrocyte
Fraction of cells in group (%)
20 40 60 80 100
Mean expression in group
0.0 0.5 1.0
column scaled expression
0.0 0.5 1.0

A

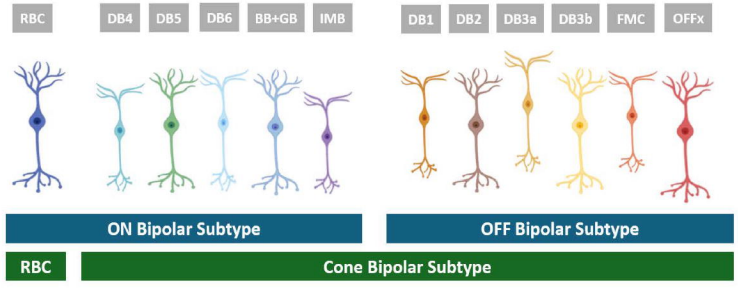
RBC
DB4
DB5
DB6
BB+GB
IMB
DB1
DB2
DB3a
DB3b
FMC
OFFx
ON Bipolar Subtype
OFF Bipolar Subtype
RBC
Cone Bipolar Subtype

B

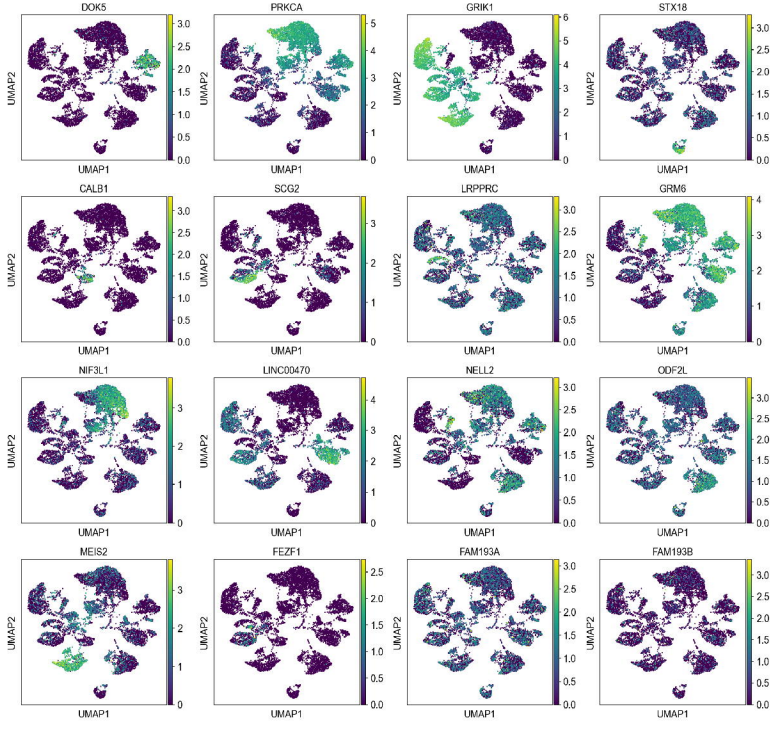
DOK5
PRKCA
GRIK1
STX18
CALB1
SCG2
LRPPRC
GRM6
NIF3L1
LINC00470
NELL2
ODF2L
MEIS2
FEZF1
FAM193A
FAM193B
UMAP1
UMAP2

C

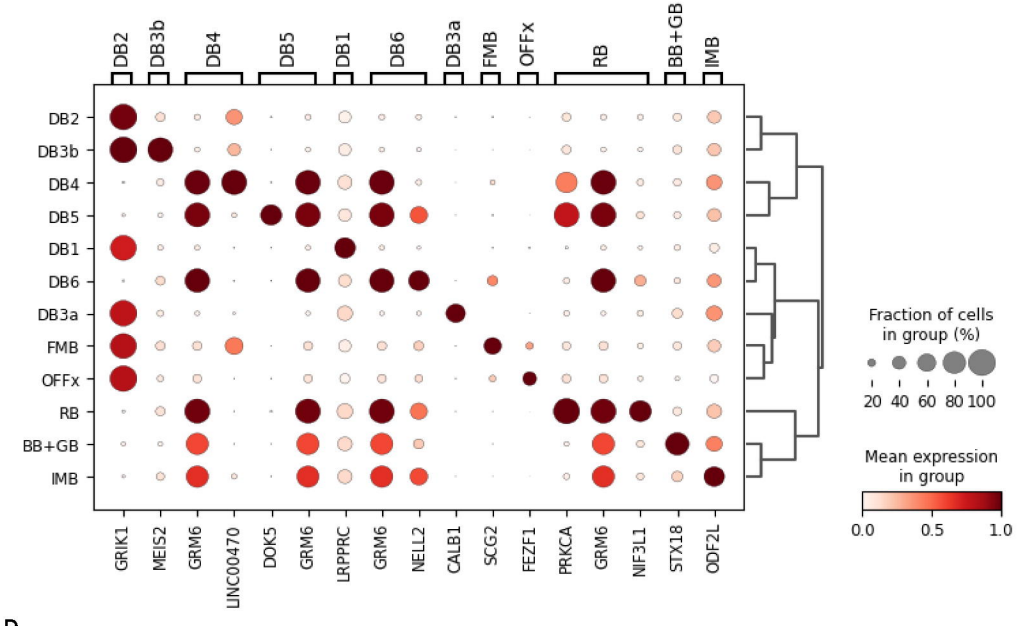
DB2
DB3b
DB4
DB5
DB1
DB6
DB3a
FMB
OFFx
RB
BB+GB
IMB
GRIK1
MEIS2
GRM6
LINC00470
DOK5
GRM6
LRPPRC
GRM6
NELL2
CALB1
SCG2
FEZF1
PRKCA
GRM6
NIF3L1
STX18
ODF2L
Fraction of cells in group (%)
20 40 60 80 100
Mean expression in group
0.0 0.5 1.0

D

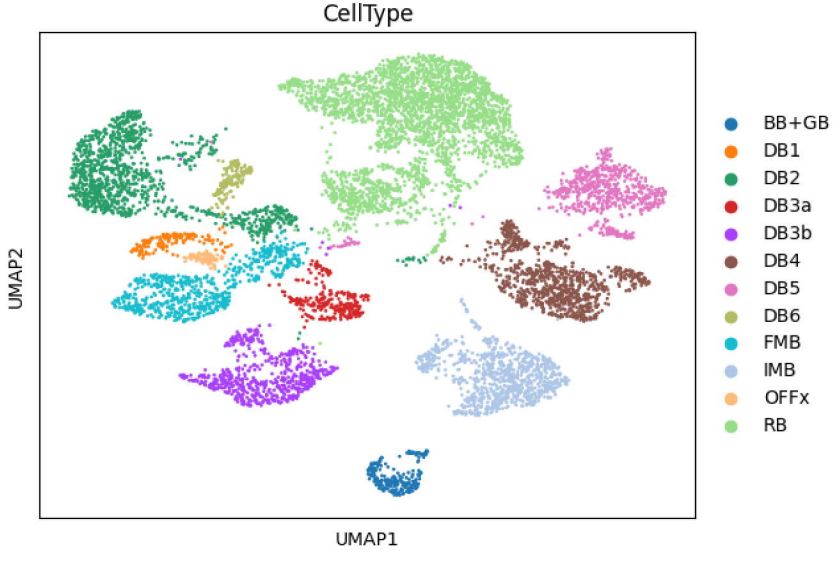
CellType
UMAP1
UMAP2
BB+GB
DB1
DB2
DB3a
DB3b
DB4
DB5
DB6
FMB
IMB
OFFx
RB

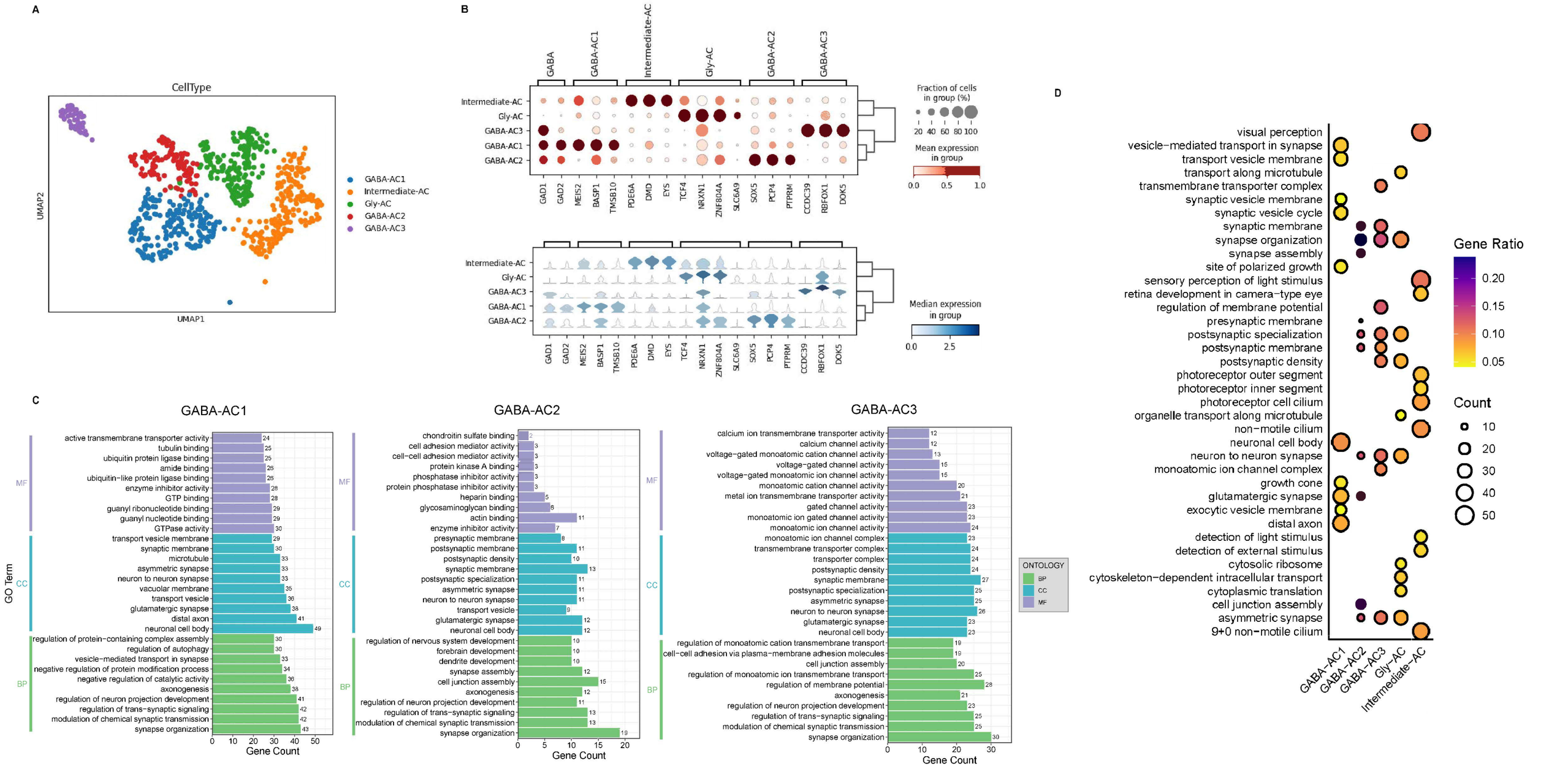
A
CellType
UMAP2
UMAP1
GABA-AC1
Intermediate-AC
Gly-AC
GABA-AC2
GABA-AC3
B
GABA
GABA-AC1
Intermediate-AC
Gly-AC
GABA-AC2
GABA-AC3
Intermediate-AC
Gly-AC
GABA-AC3
GABA-AC1
GABA-AC2
GAD1 GAD2 MEIS2 BASP1 TMSB10 PDE6A DMD EYS TCF4 NRXN1 ZNF804A SLC6A9 SOX5 PCP4 PTPRM CCDC39 RBFOX1 DOK5
Fraction of cells in group (%)
20 40 60 80 100
Mean expression in group
0.0 0.5 1.0
Median expression in group
0.0 2.5
C
GABA-AC1
GABA-AC2
GABA-AC3
GO Term
MF
CC
BP
active transmembrane transporter activity
tubulin binding
ubiquitin protein ligase binding
amide binding
ubiquitin-like protein ligase binding
enzyme inhibitor activity
GTP binding
guanyl ribonucleotide binding
guanyl nucleotide binding
GTPase activity
transport vesicle membrane
synaptic membrane
microtubule
asymmetric synapse
neuron to neuron synapse
vacuolar membrane
transport vesicle
glutamatergic synapse
distal axon
neuronal cell body
regulation of protein-containing complex assembly
regulation of autophagy
vesicle-mediated transport in synapse
negative regulation of protein modification process
negative regulation of catalytic activity
axonogenesis
regulation of neuron projection development
regulation of trans-synaptic signaling
modulation of chemical synaptic transmission
synapse organization
Gene Count
chondroitin sulfate binding
cell adhesion mediator activity
cell-cell adhesion mediator activity
protein kinase A binding
phosphatase inhibitor activity
protein phosphatase inhibitor activity
heparin binding
glycosaminoglycan binding
actin binding
enzyme inhibitor activity
presynaptic membrane
postsynaptic membrane
postsynaptic density
synaptic membrane
postsynaptic specialization
asymmetric synapse
neuron to neuron synapse
transport vesicle
glutamatergic synapse
neuronal cell body
regulation of nervous system development
forebrain development
dendrite development
synapse assembly
cell junction assembly
axonogenesis
regulation of neuron projection development
regulation of trans-synaptic signaling
modulation of chemical synaptic transmission
synapse organization
Gene Count
calcium ion transmembrane transporter activity
calcium channel activity
voltage-gated monoatomic cation channel activity
voltage-gated channel activity
voltage-gated monoatomic ion channel activity
monoatomic cation channel activity
metal ion transmembrane transporter activity
gated channel activity
monoatomic ion gated channel activity
monoatomic ion channel activity
monoatomic ion channel complex
transmembrane transporter complex
transporter complex
postsynaptic density
synaptic membrane
postsynaptic specialization
asymmetric synapse
neuron to neuron synapse
glutamatergic synapse
neuronal cell body
regulation of monoatomic cation transmembrane transport
cell-cell adhesion via plasma-membrane adhesion molecules
cell junction assembly
regulation of monoatomic ion transmembrane transport
regulation of membrane potential
axonogenesis
regulation of neuron projection development
regulation of trans-synaptic signaling
modulation of chemical synaptic transmission
synapse organization
Gene Count
ONTOLOGY
BP
CC
MF
D
visual perception
vesicle-mediated transport in synapse
transport vesicle membrane
transport along microtubule
transmembrane transporter complex
synaptic vesicle membrane
synaptic vesicle cycle
synaptic membrane
synapse organization
synapse assembly
site of polarized growth
sensory perception of light stimulus
retina development in camera-type eye
regulation of membrane potential
presynaptic membrane
postsynaptic specialization
postsynaptic membrane
postsynaptic density
photoreceptor outer segment
photoreceptor inner segment
photoreceptor cell cilium
organelle transport along microtubule
non-motile cilium
neuronal cell body
neuron to neuron synapse
monoatomic ion channel complex
growth cone
glutamatergic synapse
exocytic vesicle membrane
distal axon
detection of light stimulus
detection of external stimulus
cytosolic ribosome
cytoskeleton-dependent intracellular transport
cytoplasmic translation
cell junction assembly
asymmetric synapse
9+0 non-motile cilium
GABA-AC1
GABA-AC2
GABA-AC3
Gly-AC
Intermediate-AC
Gene Ratio
0.20
0.15
0.10
0.05
Count
10
20
30
40
50

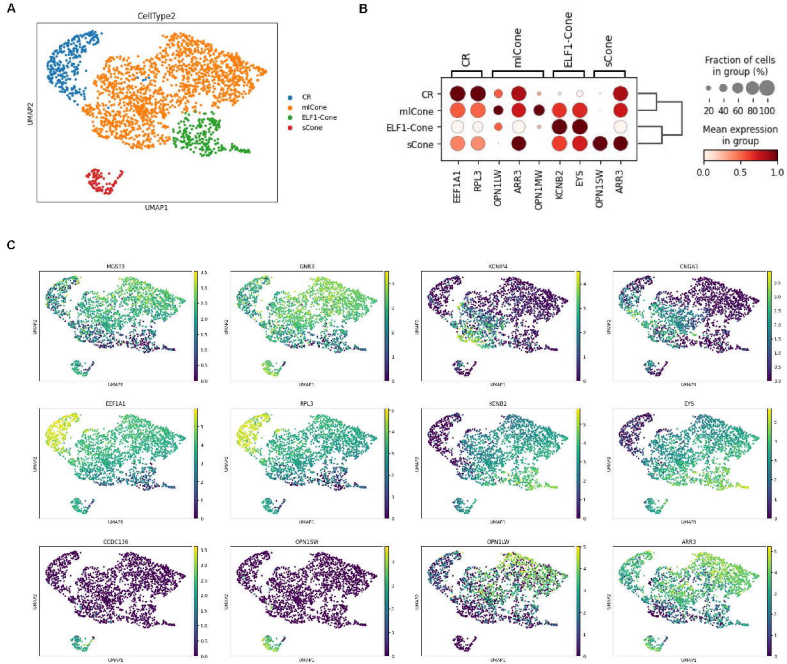
A
CellType2
UMAP2
UMAP1
CR
mlCone
ELF1-Cone
sCone
B
CR
mlCone
ELF1-Cone
sCone
EEF1A1
RPL3
OPN1LW
ARR3
OPN1MW
KCNB2
EYS
OPN1SW
ARR3
Fraction of cells in group (%)
20 40 60 80 100
Mean expression in group
0.0 0.5 1.0
C
MGST3
GNB3
KCNH4
CNGA3
EEF1A1
RPL3
KCNB2
EYS
CCDC136
OPN1SW
OPN1LW
ARR3

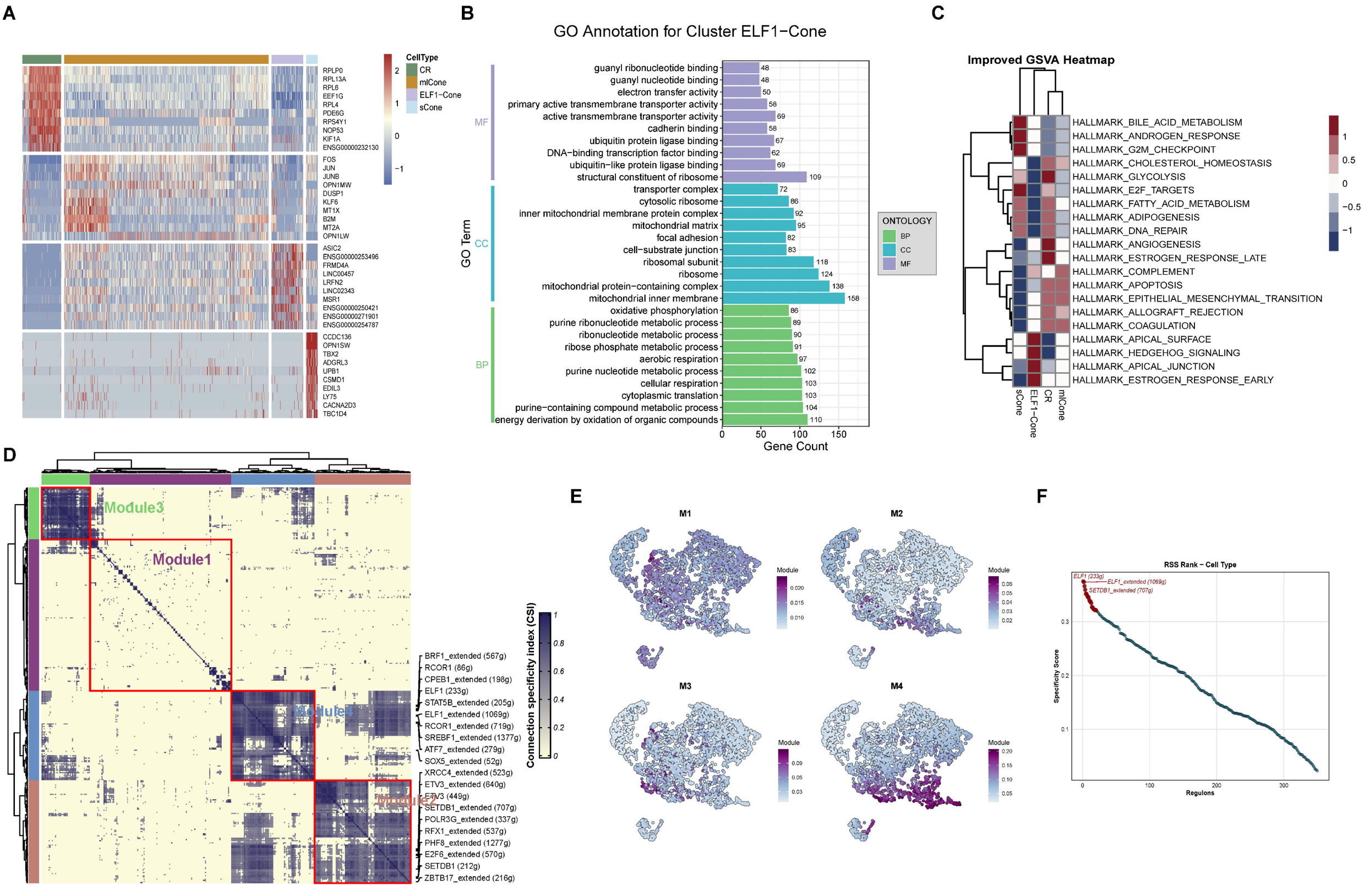
A
CellType
CR
mlCone
ELF1−Cone
sCone
RPLP0
RPL13A
RPL6
EEF1G
RPL4
PDE6G
RPS4Y1
NOP53
KIF1A
ENSG00000232130
FOS
JUN
JUNB
OPN1MW
DUSP1
KLF6
MT1X
B2M
MT2A
OPN1LW
ASIC2
ENSG00000253496
FRMD4A
LINC00457
LRFN2
LINC02343
MSR1
ENSG00000250421
ENSG00000271901
ENSG00000254787
CCDC136
OPN1SW
TBX2
ADGRL3
UPB1
CSMD1
EDIL3
LY75
CACNA2D3
TBC1D4
B
GO Annotation for Cluster ELF1−Cone
GO Term
MF
CC
BP
guanyl ribonucleotide binding
guanyl nucleotide binding
electron transfer activity
primary active transmembrane transporter activity
active transmembrane transporter activity
cadherin binding
ubiquitin protein ligase binding
DNA−binding transcription factor binding
ubiquitin−like protein ligase binding
structural constituent of ribosome
transporter complex
cytosolic ribosome
inner mitochondrial membrane protein complex
mitochondrial matrix
focal adhesion
cell−substrate junction
ribosomal subunit
ribosome
mitochondrial protein−containing complex
mitochondrial inner membrane
oxidative phosphorylation
purine ribonucleotide metabolic process
ribonucleotide metabolic process
ribose phosphate metabolic process
aerobic respiration
purine nucleotide metabolic process
cellular respiration
cytoplasmic translation
purine−containing compound metabolic process
energy derivation by oxidation of organic compounds
Gene Count
ONTOLOGY
BP
CC
MF
C
Improved GSVA Heatmap
HALLMARK_BILE_ACID_METABOLISM
HALLMARK_ANDROGEN_RESPONSE
HALLMARK_G2M_CHECKPOINT
HALLMARK_CHOLESTEROL_HOMEOSTASIS
HALLMARK_GLYCOLYSIS
HALLMARK_E2F_TARGETS
HALLMARK_FATTY_ACID_METABOLISM
HALLMARK_ADIPOGENESIS
HALLMARK_DNA_REPAIR
HALLMARK_ANGIOGENESIS
HALLMARK_ESTROGEN_RESPONSE_LATE
HALLMARK_COMPLEMENT
HALLMARK_APOPTOSIS
HALLMARK_EPITHELIAL_MESENCHYMAL_TRANSITION
HALLMARK_ALLOGRAFT_REJECTION
HALLMARK_COAGULATION
HALLMARK_APICAL_SURFACE
HALLMARK_HEDGEHOG_SIGNALING
HALLMARK_APICAL_JUNCTION
HALLMARK_ESTROGEN_RESPONSE_EARLY
sCone
ELF1−Cone
CR
mlCone
D
Module3
Module1
Module4
Module2
BRF1_extended (567g)
RCOR1 (86g)
CPEB1_extended (198g)
ELF1 (233g)
STAT5B_extended (205g)
ELF1_extended (1069g)
RCOR1_extended (719g)
SREBF1_extended (1377g)
ATF7_extended (279g)
SOX5_extended (52g)
XRCC4_extended (523g)
ETV3_extended (640g)
ETV3 (449g)
SETDB1_extended (707g)
POLR3G_extended (337g)
RFX1_extended (537g)
PHF8_extended (1277g)
E2F6_extended (570g)
SETDB1 (212g)
ZBTB17_extended (216g)
Connection specificity index (CSI)
E
M1
M2
M3
M4
Module
F
RSS Rank − Cell Type
ELF1 (233g)
ELF1_extended (1069g)
SETDB1_extended (707g)
Specificity Score
Regulons

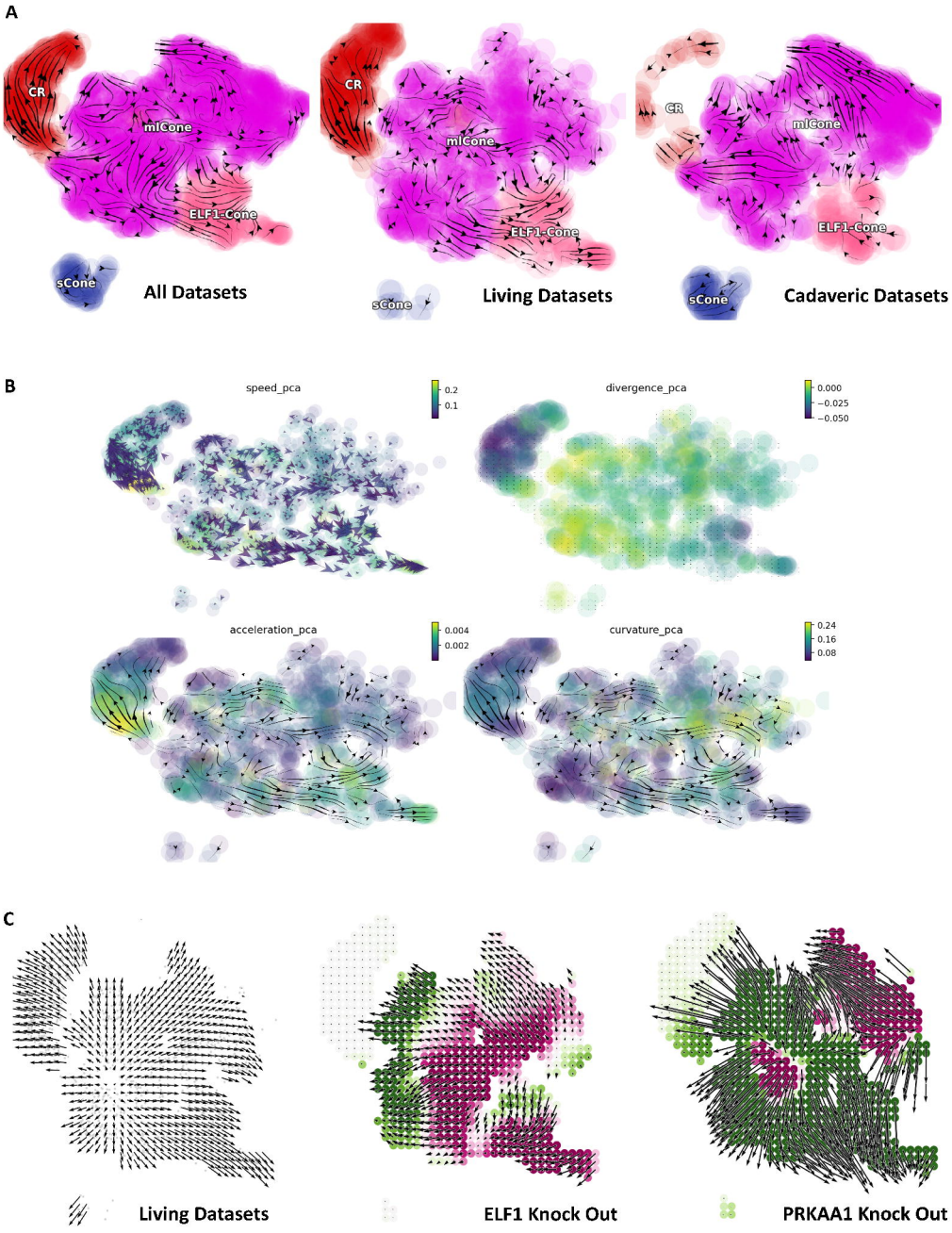
A
CR
mlCone
ELF1-Cone
sCone
All Datasets
CR
mlCone
ELF1-Cone
sCone
Living Datasets
CR
mlCone
ELF1-Cone
sCone
Cadaveric Datasets
B
speed_pca
0.2
0.1
divergence_pca
0.000
−0.025
−0.050
acceleration_pca
0.004
0.002
curvature_pca
0.24
0.16
0.08
C
Living Datasets
ELF1 Knock Out
PRKAA1 Knock Out

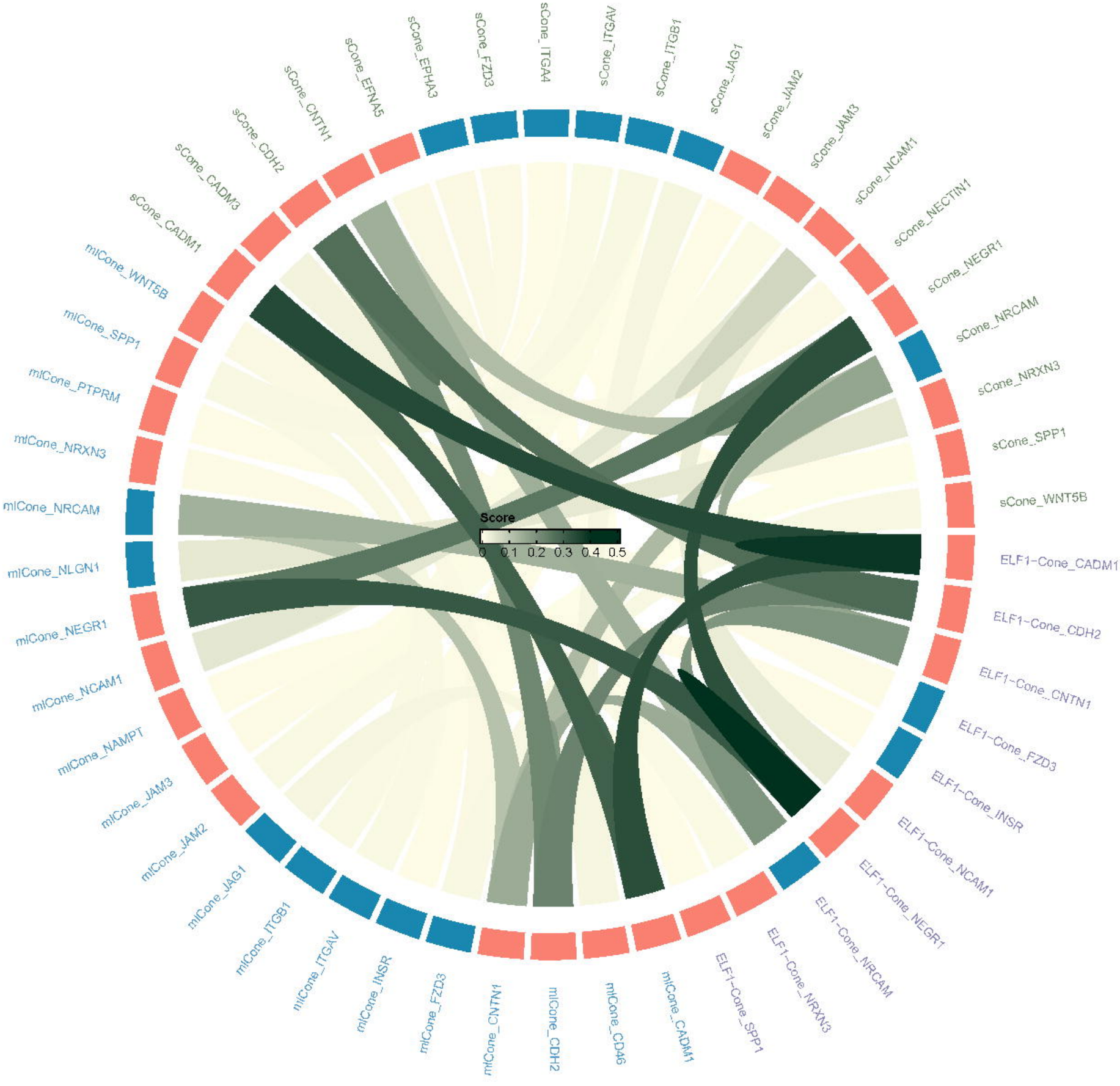
sCone_ITGA4
sCone_ITGAV
sCone_ITGB1
sCone_JAG1
sCone_JAM2
sCone_JAM3
sCone_NCAM1
sCone_NECTIN1
sCone_NEGR1
sCone_NRCAM
sCone_NRXN3
sCone_SPP1
sCone_WNT5B
ELF1-Cone_CADM1
ELF1-Cone_CDH2
ELF1-Cone_CNTN1
ELF1-Cone_FZD3
ELF1-Cone_INSR
ELF1-Cone_NCAM1
ELF1-Cone_NEGR1
ELF1-Cone_NRCAM
ELF1-Cone_NRXN3
ELF1-Cone_SPP1
mlCone_CADM1
mlCone_CD46
mlCone_CDH2
mlCone_CNTN1
mlCone_FZD3
mlCone_INSR
mlCone_ITGAV
mlCone_ITGB1
mlCone_JAG1
mlCone_JAM2
mlCone_JAM3
mlCone_NAMPT
mlCone_NCAM1
mlCone_NEGR1
mlCone_NLGN1
mlCone_NRCAM
mlCone_NRXN3
mlCone_PTPRM
mlCone_SPP1
mlCone_WNT5B
sCone_CADM1
sCone_CADM3
sCone_CDH2
sCone_CNTN1
sCone_EFNA5
sCone_EPHA3
sCone_FZD3
Score
0 0.1 0.2 0.3 0.4 0.5

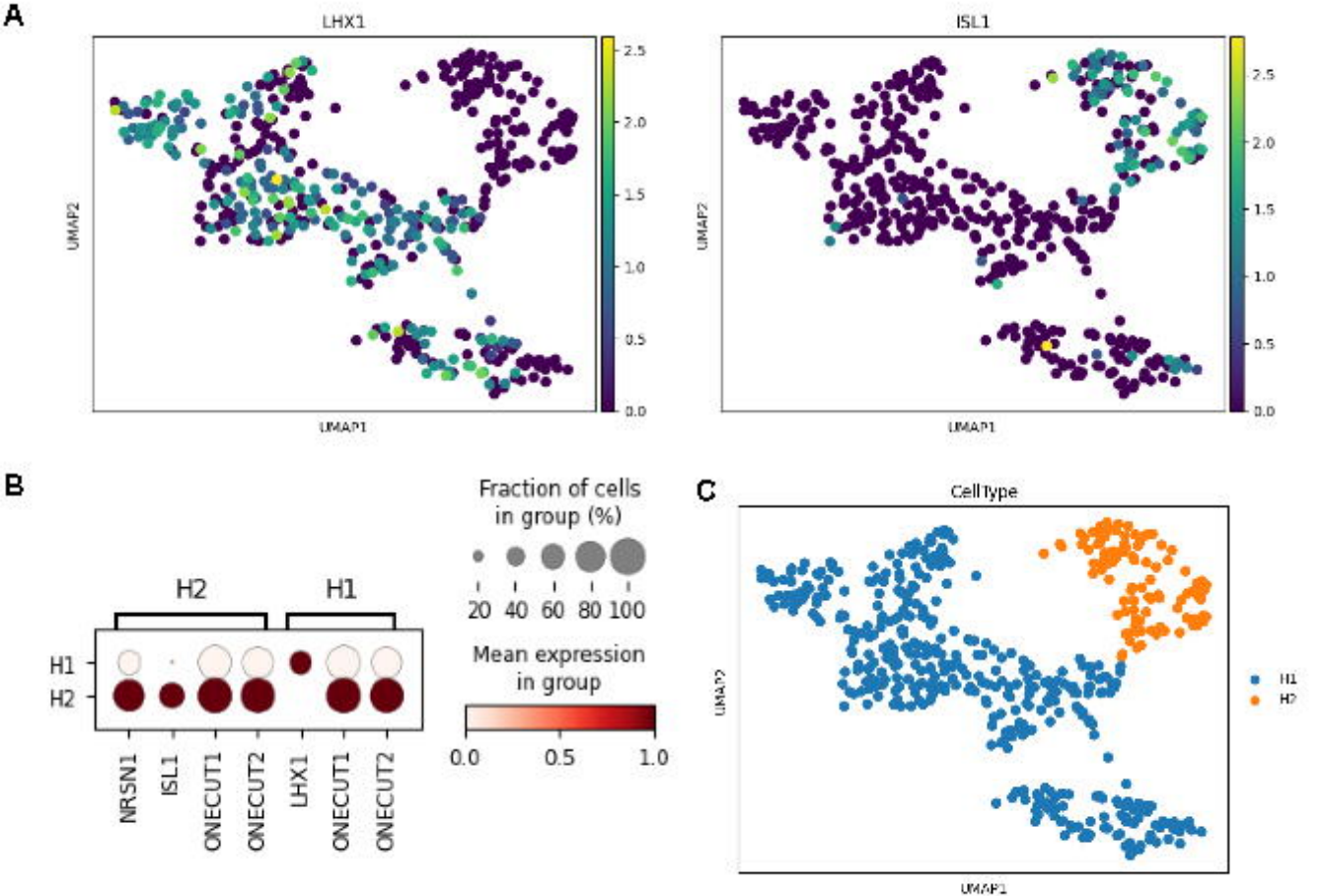
A
LHX1
ISL1
UMAP2
UMAP1
2.5
2.0
1.5
1.0
0.5
0.0
B
H2
H1
NRSN1
ISL1
ONECUT1
ONECUT2
LHX1
ONECUT1
ONECUT2
Fraction of cells in group (%)
20 40 60 80 100
Mean expression in group
0.0 0.5 1.0
C
Cell type
H1
H2

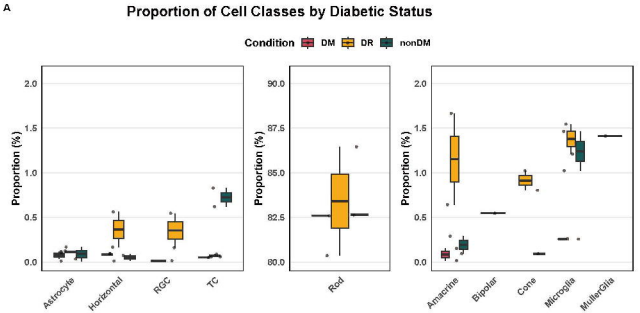
A
Proportion of Cell Classes by Diabetic Status
Condition DM DR nonDM
Proportion (%)
Astrocyte
Horizontal
RGC
TC
Rod
Amacrine
Bipolar
Cone
Microglia
MullerGlia

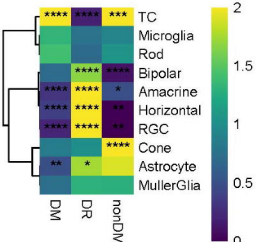
B
TC
Microglia
Rod
Bipolar
Amacrine
Horizontal
RGC
Cone
Astrocyte
MullerGlia
DM
DR
nonDM

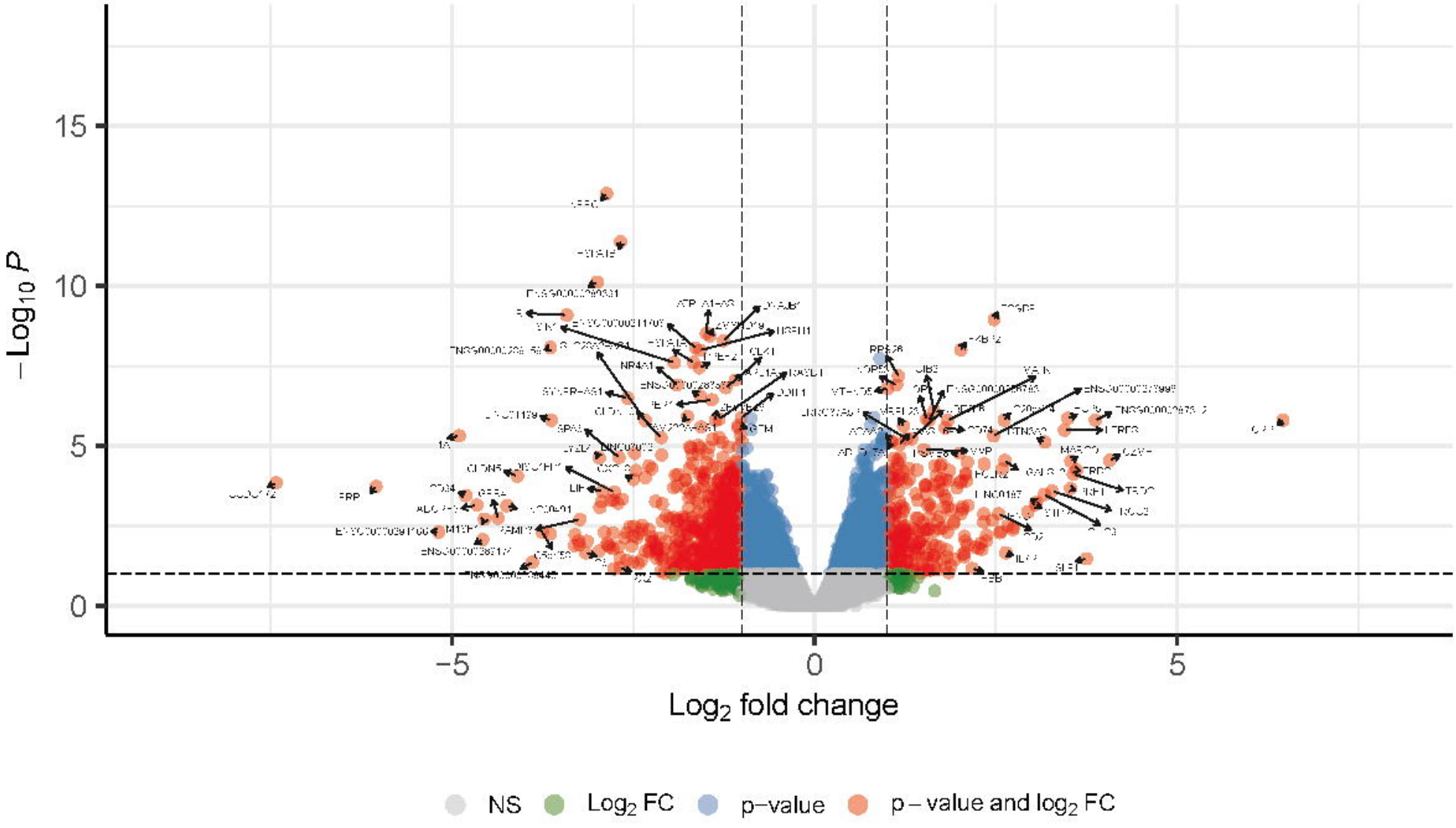
15
10
5
0
−Log10 P
−5
0
5
Log2 fold change
NS
Log2 FC
p−value
p − value and log2 FC
total = 16261 variables